

1 **Title:** Modeling nonlinear tidal evolution in an energetic estuary

2 Salme Cook<sup>\*,a</sup>, Thomas C. Lippmann<sup>a</sup>, and James D. Irish<sup>a</sup>

3 <sup>a</sup>University of New Hampshire, 24 Colovos Rd., Durham, NH 03824, United States of America.

4 <sup>\*</sup>Corresponding Author: Salme Cook, sc10@wildcats.unh.edu

5

6 **Abstract**

7 Three-dimensional numerical simulations of a tidally dominated estuary within the Gulf of  
8 Maine are performed using the Regional Ocean Modeling System (ROMS) and validated with  
9 observations of sea surface elevation and velocity time series obtained between 1975 and 2016.  
10 The model is forced at the ocean boundary with tidal constituents (M2, S2, N2, O1, K1), a time  
11 series of observed subtidal elevations and discharge from seven rivers that drain into the estuary.  
12 Harmonic analysis is used to determine the tidal dissipation characteristics and generation of  
13 overtides within the system. Amplitude decay and phase shift of the dominant semidiurnal (M2)  
14 tidal component shows good agreement with observations throughout the main channel of the  
15 Piscataqua River and over the channels and mudflats of the Great Bay. The model simulates  
16 harmonic growth of the overtides across the spectrum, and indicates a spatial evolution of the  
17 tide consistent with a shoaling wave that evolves from a skewed elevation profile with ebb  
18 dominance in the lower parts of the estuary, to a more asymmetric, pitched-forward shape  
19 consistent with flood dominance. The M4 constituent has spatial variation qualitatively similar  
20 to the observations but has magnitudes that are under-predicted in the complex bathymetric  
21 region of the Piscataqua River where much of the M2 tidal dissipation occurs. The M6 tidal  
22 constituent agrees well with the observations throughout the estuary suggesting that frictional  
23 effects on harmonic growth are well modeled. Root-mean-square model-data differences in  
24 velocities ( $\sim 0.05$  m/s) and sea surface elevation ( $\sim 0.1$  m) agree to within about 10% of the tidal

25 amplitudes. Differences between model simulations with and without subtidal oscillations in the  
26 estuary are small, suggesting that interactions between the tide and other low frequency  
27 (subtidal) mean flows are weak and can be ignored when considering tidal dynamics. Including  
28 average fresh water discharge in the model does not affect the behavior of the tidal flows, but can  
29 generate high frequency baroclinic velocities potentially important to mixing within the estuary.

30

### 31 **Keywords**

32 numerical modeling

33 tidal dissipation

34 nonlinear tidal evolution

35 Gulf of Maine

36 hydrodynamic model validation

37

### 38 **1. Introduction**

39         The transport and mixing of water, sediment, nutrients and organisms in estuarine and  
40 coastal systems is often dominated by astronomical tidal forcing. Of particular interest are the  
41 dynamics of shoaling tides induced by nonlinear wave interactions and energy dissipation, and  
42 how that process impacts long term coastal planning and environmental conservation efforts. As  
43 the tide propagates from the open ocean onto the shelf and into estuaries, it becomes  
44 progressively more nonlinear and distorted, leading to growth (shoaling) or decay (dissipation)  
45 of tidal amplitudes, shifts in the phase of the tide, and growth of tidal harmonics. Resulting tidal  
46 currents are difficult to predict analytically over realistic and complex bathymetry, and require  
47 observation or numerical simulation to quantify. Evolution of tidal nonlinearities produces  
48 asymmetries in ebb/flood current strength and duration (Boon and Byrne, 1981), that when  
49 averaged over a tidal cycle has been used to estimate net sediment transport and circulation

50 patterns (Dronkers, 1986); stronger flood currents drive the movement of coarse sediment and  
51 longer slack periods promote the deposition of fine-grained sediment.

52 Tidal amplitude attenuation in an estuary occurs from energy losses due to turbulent  
53 mixing and from frictional effects due to interactions with the bottom and lateral boundaries of  
54 the estuary. Energy dissipation of the tidal wave can be described in terms of amplitude decay of  
55 the dominant tidal constituent, which for the Gulf of Maine is the semi-diurnal M2 tide that  
56 contributes about 90% of the predicted tidal variance. Not all energy is dissipated due to  
57 frictional effects, and some is transferred to higher harmonics (overtides; *e.g.*, the M4 and M6  
58 tidal constituents) through nonlinear interactions and frictional effects that create tidal  
59 asymmetry (Aubrey and Speer, 1985; Speer and Aubrey, 1985; Parker, 1991). A comparison of  
60 the magnitude of the M2 constituent with the first harmonic M4 is a direct measure of nonlinear  
61 interactions of the M2 tide, whereas the phase difference qualitatively describes the tidal  
62 asymmetries in the system (Friedrichs and Aubrey, 1988). Generation of the M6 component is  
63 largely attributed to frictional effects (Parker, 1991).

64 The dissipation problem is complicated by the highly nonlinear nature of tidal shoaling  
65 and propagation, and the need to define representative bottom boundary conditions that  
66 characterize the interactions between tidal currents and the seabed. Dissipation in inlets and  
67 estuaries leads to development of local phase lags between pressure and velocities that shift slack  
68 tide periods up to a quarter of the wave period (90 *deg* phase shifts between sea surface elevation  
69 and along channel velocity), and also impacts the evolution of tidal harmonics that are amplified  
70 and phase-shifted relative to open ocean values. This behavior can affect the overall transport in  
71 the estuary, thus a good understanding of the spatial and temporal patterns in tidal dissipation can

72 aid in long-term coastal management and planning, for example site selection for tidal renewable  
73 energy projects (Neill, *et al.*, 2014).

74         The tides may also interact nonlinearly with river flow, storm surges and wind driven  
75 currents that vary on time scales of hours to months. Often observations from only a few  
76 locations are used to describe the overall dynamics of an estuary, and field experiments are  
77 limited to one specific area for a discrete amount of time. It is often not feasible to collect  
78 enough measurements continuously everywhere to adequately characterize the tides and  
79 associated flows; thus, numerical models can be used to produce system-wide predictions of  
80 water levels and currents under different hydrodynamic and meteorological forcing conditions  
81 (*e.g.*, Warner, *et al.*, 2005a). Quantitative prediction of tidal amplitudes and currents is needed for  
82 flooding and inundation studies, mooring and berthing design, safe navigation, interaction with  
83 structures, and bottom shear stress prediction for sediment transport, organism transport and  
84 nutrient fluxes.

85         In this study, we discuss the implementation and validation of a three-dimensional high-  
86 resolution hydrodynamic model of a tidally dominated well-mixed estuary located within the  
87 Gulf of Maine. The Gulf of Maine has a natural resonance close to the semidiurnal (M2) tidal  
88 constituent (Garrett, 1972), enhancing the tides throughout the gulf, including connected  
89 estuaries and coastal embayments including the Bay of Fundy. In this study we examine the  
90 Piscataqua River - Great Bay estuary located within the Gulf of Maine at the border of New  
91 Hampshire and Maine (Figure 1). Tidal forcing for the Great Bay is dominated by the  
92 semidiurnal (M2) component of the tide, has a tide range on the order of 2-4 *m* (depending on the  
93 spring-neap cycle), and has variable (but mostly minor) freshwater river discharge. It is home to  
94 both the second deepest U.S. naval port, and Portsmouth Harbor, which is home to some of the

95 fastest tidal currents of any commercial port on the U.S. East Coast. The estuary has two tidal  
96 regimes: a high dissipative region through the lower Piscataqua River from the mouth to Dover  
97 Point, and a low dissipative regime from Dover Pt. through the Little Bay and Great Bay (Brown  
98 and Trask, 1980; Swift and Brown, 1983). The former region behaves like a partially progressive  
99 wave with concomitant phase shift of the slack tidal period, whereas the latter has phase shifts  
100 consistent with standing waves. This behavior causes changes in the timing of tidal currents and  
101 the associated net sediment transport throughout the estuary. Previous modeling studies of the  
102 Great Bay (Ip, *et al.*, 1998; Erturk, *et al.*, 2002; McLaughlin, 2003) considered depth-integrated,  
103 two dimensional flow fields, with the primary focus of representing the gross tidal behavior to  
104 estimate the net transport of water and sediment in the estuary.

105         The model validation process includes examination of the nonlinear tidal behavior that  
106 drives tidal asymmetry and tidal energy dissipation in terms of amplitude decay and phase lags  
107 using water level measurements and harmonic analysis. Modeled results are compared with  
108 coincident and previous observations, and with results from the literature. This study will form  
109 the basis for additional modeling aimed at examining the spatial variation in bottom shear  
110 stresses needed for sediment transport calculations, horizontal and vertical mixing within the  
111 estuary, and transport of larvae, nutrients and carbon within the estuary.

112         Section 2 describes the field site, observational datasets, the hydrodynamic model and  
113 grid development, and the model validation and tidal analysis methodology. Section 3 describes  
114 model results, and Section 4 discusses the model-observation comparison in terms of nonlinear  
115 evolution. Section 5 presents the conclusions of the study.

## 116 **2. Methods**

### 117 **2.1 Site Description**

118           The Great Bay Estuarine system is located along the New Hampshire-Maine border  
119 within the Gulf of Maine in the northeastern portion of the United States (Figure 1). It is a  
120 recessed, drowned river valley connected to the Gulf of Maine via the Piscataqua River  
121 (Armstrong, *et al.*, 1976). The tide range is 2-4 *m* over the spring-neap cycle with tidal currents  
122 greater than 2 *m/s* in the channels at maximum ebb and flood tides. At low tide as much as 50%  
123 of the Great Bay is exposed as low-lying mudflats, cut with deep tidal channels. The surface area  
124 of the estuary is approximately 55 *km*<sup>2</sup> measured at mean high water (NHDES, 2007). The  
125 volume is 156·10<sup>6</sup> *m*<sup>3</sup> and 235·10<sup>6</sup> *m*<sup>3</sup> for low and high tides respectively, with a tidal prism of  
126 79·10<sup>6</sup> *m*<sup>3</sup> (Swift and Brown, 1983; NHDES, 2007). Seven tributaries contribute fresh water to  
127 the system: the Squamscott, Lamprey, Winnicut, Oyster, Bellamy, Cocheco, and Salmon Falls,  
128 all feeding the Upper and Lower Piscataqua river that flows into the Gulf of Maine. River fluxes  
129 are determined by precipitation and runoff and regulated by dams or weirs that modulate the  
130 freshwater volume entering the system. Typically (except during large storms or the spring melt),  
131 the freshwater input is relatively small and only contributes 2% of the tidal prism (Short, 1992;  
132 NHDES, 2007). The generally small freshwater fluxes and strong tidal mixing results in weak or  
133 negligible stratification (except very close to the river mouths) and during periods of little  
134 rainfall the salinities at the Great Bay Buoy (Figure 3) are nearly equal to the Gulf of Maine  
135 indicating that horizontal variation in density due to river fluxes are also weak. As our interests  
136 include the ability of the numerical model to represent the vertically varying flow fields, we will  
137 include model runs with and without average river discharges to evaluate the influence of  
138 baroclinic flows on the tidal behavior.

139           Ocean waves outside the mouth of the estuary are strongly refracted away from the deep  
140 center channel and rapidly attenuate upstream, and thus do not greatly contribute to the velocities

141 or water level fluctuations in the estuary, other studies have shown that waves can have an  
142 impact on tidal currents (*e.g.*, Lewis, et al., 2014). Wind-driven surface gravity waves in the  
143 large lobe of the Great Bay proper are generally small (5-20 *cm* significant heights) owing to the  
144 limited fetch and strong attenuation by energy loss through interactions with tidal currents and  
145 the muddy bottom or shallow aquatic vegetation (eel grass meadows). Although waves on the  
146 Great Bay could be important to bottom shear stresses over the mud flats, they do not  
147 substantially alter the larger scale circulation, and thus are not considered further in this study.  
148 Wind-driven mean currents may be substantial during storm conditions, but are generally much  
149 weaker than the tidal currents (Wengrove, *et al.*, 2015) and thus are also not considered in this  
150 study.

151 The bathymetry of the estuary is complex (Figure 2), with steep sidewalls in the main  
152 channel of the Piscataqua River with water depths ranging 13-26 *m*. Ocean water flows into  
153 mouth of the Piscataqua River through two channels, a main entry point to the north of New  
154 Castle Island between New Hampshire and Maine, and a secondary entry point through Little  
155 Harbor to the south of New Castle. Tides entering Little Harbor flow through relatively shallow  
156 water and around several islands, and join the Piscataqua River between Pierce Island and  
157 Portsmouth, NH. Flows through the main channel make a sharp 90 *deg* turn around New Castle  
158 at Fort Point, and then flow around the Portsmouth Naval Shipyard primarily to the south in the  
159 deeper channel but also the back bay, a narrow, shallow waterway that reconnects with the  
160 Piscataqua River near Pierce Island. The Piscataqua River splits at Dover Pt., with the main  
161 flows sharply turning south into Little Bay, and with a smaller portion of the flow heading to the  
162 north connecting the lower Piscataqua River with the Upper Piscataqua fed by the Cocheco, and

163 Salmon Falls rivers to the north, with average summer discharge rates of 8.54 and 15.4  $m^3/s$ ,  
164 respectively (NHDES, 2007).

165 The channel between the mouth at New Castle Island and Dover Pt. is 12 km long and  
166 characterized by a hard rocky bottom with coarse sediment in the deep channels and steep rocky  
167 shorelines for most of the reach. The flows through this part of the estuary are high (exceeding 2  
168  $m/s$  in some locations) on both the flood and ebb tides. Once the flow enters the Little Bay it  
169 remains strong through the deep center channels with weaker flows up and over the bordering  
170 mud flats. The Oyster and Bellamy rivers that flow into the Little Bay have average summer  
171 discharges of 0.94 and 1.32  $m^3/s$ , respectively (NHDES, 2007). The Little Bay joins the Great  
172 Bay at Furber Strait near Adam's Pt. The deep center channel gradually shallows and bifurcates  
173 into an eastern and western branch flanked by large mud flats that dominate this portion of the  
174 estuary. The Squamscott, Lamprey, and Winnicut rivers all flow into this part of the estuary,  
175 with average summer discharge rates of 5.3, 10.0, and 0.7  $m^3/s$ , respectively (NHDES, 2007).  
176 For this study, the tidal analysis focuses on the main channel flows from the mouth of the  
177 Piscataqua River to the upper reaches (Squamscott River) of the Great Bay estuary (Figure 1).

## 178 **2.2 Observations**

179 Field observations of horizontal currents spanning the water column and sea surface  
180 elevation (from bottom pressure and tidal stations) were obtained during several field  
181 experiments in 1975, 2007, 2009, 2015, and 2016, and the continuously operating NOAA Tide  
182 Gauge station at Fort Point, NH (Station ID: 8423898). Table 1 summarizes the dates and  
183 durations of the field studies and Figure 3 shows the instrument locations.

184 Observations of tidal elevations and currents within the estuary were obtained in 1975 by  
185 the University of New Hampshire (UNH) in cooperation with the National Ocean Survey (NOS;



186 summarized in Swenson *et al.*, 1977 and Silver and Brown, 1979). Original data were  
187 unavailable so tidal analysis estimating M2 tidal amplitudes and phases from Swift and Brown  
188 (1983) is used in this study. Observations of bi-directional currents (in 0.5 – 1.0 *m* range bins)  
189 and water levels from the mouth to Adams Pt. were obtained by NOAA in 2007 using six  
190 bottom-mounted, upward-looking acoustic Doppler current profilers (ADCPs). The instruments  
191 were deployed for between 41 and 45 days, recovered, and then moved to new locations with  
192 water depths ranging between 4.3 and 19.3 *m*. These data are available and described online at  
193 <https://tidesandcurrents.noaa.gov>. Observations of water levels were obtained by UNH in 2009 at  
194 four locations in the Great Bay using bottom mounted pressure sensors and an RTK GPS buoy.  
195 The instruments were sampled between 30 and 120 *s* and deployed between 9 and 84 days, and  
196 averaged over 6 *min* intervals following standard NOAA procedures. Observations obtained for  
197 7 – 71 days by UNH in 2015 and 2016 include 1 *min* averaged bi-directional currents (in 0.25 –  
198 1.0 *m* range bins) and water levels from six ADCPs deployed across the Great Bay in water  
199 depths ranging 3 – 17 *m*. Bottom pressure was converted to sea surface elevation using observed  
200 bottom temperature at the instrument location and salinity obtained from the Great Bay Coastal  
201 Buoy located in the center of the Great Bay Estuary  
202 ([http://www.opal.sr.unh.edu/data/buoys/great\\_bay/index.shtml](http://www.opal.sr.unh.edu/data/buoys/great_bay/index.shtml)).

### 203 **2.3 Hydrodynamic Model**

204 The Regional Ocean Modeling System (ROMS, Haidvogel *et al.*, 2008; Shchepetkin and  
205 McWilliams, 2005) is an ortho-curvilinear three-dimensional numerical coastal ocean circulation  
206 model that solves finite-difference approximations of the Reynolds-averaged Navier Stokes  
207 (RANS) equations using the hydrostatic and Boussinesq assumptions. The objectives of this  
208 study focus on the hydrodynamic component to determine the tidal dynamics, which are of first

209 order concern in validating the numerical model. ROMS has been used in both regional (*e.g.*,  
210 Zhang, *et al.* 2009; Yang, *et al.* 2016) and estuarine modeling studies (*e.g.*, Warner, *et al.* 2005a;  
211 Moriarty, *et al.*, 2014), and implemented into other coupled modeling systems (*e.g.*, Warner, *et*  
212 *al.*, 2008; Warner, *et al.*, 2010).

213 A third order upwind advection scheme is used to solve for horizontal advection. A  
214 centered-fourth order advection scheme is used to solve for vertical advection. A  $k$ - $\epsilon$  generic  
215 length scale (GLS) turbulence closure model is used to calculate the horizontal and vertical eddy  
216 viscosities (Umlauf and Burchard, 2003; Warner, *et al.*, 2005b) in conjunction with the Kantha  
217 and Clayson (1994) stability function. Within ROMS the wetting and drying algorithm (Warner,  
218 *et al.*, 2013) is utilized to simulate the inundation and draining of the tide over shallow areas  
219 alternatively covered and uncovered by the tide, in which the critical depth ( $D_{crit}$ ) is set to 10 *cm*.  
220 Once the total water depth is less than  $D_{crit}$ , no flux is allowed out of that cell and it is considered  
221 “dry”. Finally, barotropic and baroclinic modes are solved separately in ROMS with the mode-  
222 splitting algorithms described in Haidvogel, *et al.* (2008). Barotropic time steps in model  
223 simulations herein are 1/20 of the baroclinic time step.

### 224 **2.3.1 Model Grid**

225 The model domain is defined by a rectilinear Arakawa “C” grid with a constant 30-by-30  
226 *m* horizontal resolution (Figure 4; downsized by a factor of 33 1/3 in the figure). There are 8  
227 vertical layers in a terrain-following ( $\sigma$ ) coordinate system that is adjusted for slightly higher  
228 resolution near the surface and bottom boundaries. The domain is rotated 37 *deg* CCW from true  
229 north to align the offshore boundary with the approximate orientation of the shoreline along the  
230 New Hampshire-Maine coast. The domain ranges 22.02 by 25.02 *km* (734 by 834 cells). The  
231 grid elevations were defined using bathymetric data obtained from the Center for Coastal and

232 Ocean Mapping (CCOM; <http://ccom.unh.edu>), and LIDAR data collected by USGS, NOAA,  
233 and USACE (<https://coast.noaa.gov/dataviewer>), and interpolated onto the center of the  
234 horizontal grid cells. A hierarchy was defined that weighted the most accurate, recent, and  
235 complete topographic and bathymetric data highest, with any gaps filled with more uncertain,  
236 older, or less complete data sources. The combined elevation grid (Figure 4) was then processed  
237 with the MATLAB Easygrid routine (<https://www.myroms.org/wiki/easygrid>) to create the  
238 rectilinear grid and corresponding land mask that was subsequently input into ROMS. During  
239 model testing, the grid was smoothed in locations sensitive to numerical instabilities using  
240 interpolation methods described in Plant, *et al.* (2002).

### 241 **2.3.2 Boundary Conditions**

242 At the open ocean boundary (south edge of the rotated domain; Figure 4) the model is  
243 forced by tidal and subtidal oscillations (see Section 2.3.3) using the implicit Chapman (free  
244 surface) and Flather (depth averaged velocity) boundary conditions. The Chapman-Flather  
245 conditions employ the radiation method at the boundary, assuming all outgoing signals leave at  
246 the shallow water wave speed (Flather, 1976; Chapman, 1985). These particular boundary  
247 conditions have been shown to be the most suitable for tidal forcing (Palma and Matano, 1998,  
248 2000; Marchesiello, *et al.*, 2001; Carter and Merrifield, 2007). Three-dimensional baroclinic  
249 momentum equations were set to radiation and gradient conditions for velocities and tracers. The  
250 eastern, northern, and western edges of the domain are closed.

251 The bottom boundary condition for momentum was parameterized by a simple drag  
252 coefficient assuming a logarithmic vertical velocity profile in the bottom vertical cell. The drag  
253 coefficient,  $C_D$ , is represented by

254 
$$C_D = \left( \frac{\kappa}{\ln(z/z_{ob})} \right)^2 \quad (1)$$

255 where  $z$  is the vertical elevation of the mid-point of the bottom cell,  $z_{ob}$  is a characteristic bottom  
 256 roughness (in  $m$ ), and  $\kappa = 0.41$  is the von Karman coefficient (Kundu, 1990). A range of bottom  
 257 roughness values (from 0.015 – 0.030  $m$ ) were tested and the best fit was determined iteratively  
 258 from model-data comparisons of M2 tidal dissipation as a function of distance from the estuary  
 259 mouth (see Figure 5). Within each run,  $z_{ob}$  was assumed to be spatially uniform across the  
 260 domain. The kinematic bottom stress boundary conditions are given by

261 
$$\tau_b^x = \rho_0 C_D u \sqrt{u^2 + v^2} \quad (2)$$

262 
$$\tau_b^y = \rho_0 C_D v \sqrt{u^2 + v^2} \quad (3)$$

263 where  $\tau_b^x$  and  $\tau_b^y$  are the bottom stresses in the  $x$  and  $y$  directions, respectively.

264 **2.3.3 Model Initialization and Forcing**

265 Forcing conditions at the open ocean boundary are specified in two ways. The first is  
 266 with an analytical representation of tidal elevations and velocities considering only the principal  
 267 semidiurnal (M2, N2, S2) and diurnal (O1, K1) tidal constituents determined by the Oregon State  
 268 University global Tidal Prediction Software package (OTPS) in conjunction with the United  
 269 States East Coast regional Tidal Solution (EC2010; Egbert and Erofeeva, 2002). The OTPS  
 270 provided the necessary tidal amplitude and phases that correspond to the observational datasets  
 271 for the 2015 field study used in the model-data comparisons of velocities (see Section 2.4.2 and  
 272 Figure 6). The amplitudes and phases compared favorably with a harmonic analysis of observed  
 273 water level fluctuations at Fort Pt. for the 2015 field experiment using T\_TIDE (Pawlowicz, *et*  
 274 *al.*, 2002).

275           The second forcing consists of the analytical representation of the tides and including  
276   subtidal oscillations associated with atmospheric motions obtained from low-pass filtered (with a  
277   33 *hr* cut-off period) observed time series of 6-minute averaged water levels at the Fort Pt. tidal  
278   station. The subtidal motions can have amplitudes in the Gulf of Maine of 0.10-0.30 *m* (Brown  
279   and Irish, 1992), change the water depth over the shallow mudflats considerably, and although  
280   the time scales of the oscillations are generally much longer than the dominant semidiurnal tides,  
281   may contribute to the overall water velocities on the flood and ebb. Coastal ocean currents  
282   associated with barometric, wind-driven, or other shelf motions at the offshore open boundary  
283   are assumed small (consistent with observations of currents from 2007 at the most seaward  
284   instrument location, PIR0701) and not considered herein.

285           In each case (tidal with or without subtidal forcing), time series of water level  
286   fluctuations are ramped hyperbolically from rest over a 2-day period. Although tidal currents are  
287   included at the open boundary, test simulations in which the boundary currents were set to zero  
288   and allowed to evolve with the sea surface fluctuations did not alter the results, suggesting that  
289   approximating the forcing by only the pressure gradient at the mouth is reasonable (consistent  
290   with Geyer and MacCready, 2014). Time series of at least 32 days are used to force the model  
291   so that tidal analysis with T\_TIDE produces amplitudes and phases of the dominant tidal  
292   constituents (with confidence intervals). The open ocean boundary is located about 7.5 *km* from  
293   the mouth of the estuary where the Fort Pt. tide station is located. The time for the tide wave to  
294   propagate this distance is small, about 7.3-8.1 *min* based on an average water depth of 30-24 *m*,  
295   and thus has small effect on the phase estimates (about 3.3-3.9 *deg*) when comparing to  
296   coincident observations within the estuary.

297            Three-dimensional simulations were performed both with and without freshwater flows  
298 based on the average summer river discharge (see Section 2.1), salinity (varying between 6.93  
299 and 23.54 *psu*), and water temperature (varying between 19.5 and 25.4 *deg. C*) for the various  
300 rivers for the summer of 2015 was provided by the New Hampshire Department of  
301 Environmental Services  
302 (<https://www.des.nh.gov/organization/divisions/water/wmb/vrap/data.htm>). Ocean water  
303 temperature (17 *deg. C*) and salinity (31.5 *psu*) was assumed constant and given by typical  
304 summer values for the Gulf of Maine. Diurnal surface heating and cooling were assumed small  
305 in comparison to the tidal mixing and were ignored. Although the precise values of the  
306 fluctuating river discharge, temperature, and salinity were not used in the model, the variations in  
307 temperature and salinity predicted by the model compare favorably with 2015 observations  
308 obtained in the middle of the Great Bay near the surface with the Great Bay Coastal Buoy  
309 ([http://www.opal.sr.unh.edu/data/buoys/great\\_bay/index.shtml](http://www.opal.sr.unh.edu/data/buoys/great_bay/index.shtml)) and near the bottom with the  
310 SeaBird instruments co-located with our ADCP's deployed in 2015. Modeled and observed  
311 fluctuations in temperature and salinity follow tidal cycles and reveal weak vertical gradients in  
312 temperature (about 1-2 *deg. C*) and salinity (about 1-2 *psu*), consistent with a well-mixed Great  
313 Bay environment away from the river mouths during typical summer conditions in New  
314 Hampshire.

315            Model simulations including subtidal oscillations and river fluxes had a very weak effect  
316 on the tidal behavior and thus the results presented below will focus on the model simulations for  
317 barotropic tides. This is not unexpected for the typical summer conditions examined herein, but  
318 might be an important consideration during extreme storms and high runoff periods or in the  
319 very shallow depths near the water's edge over the mudflats. The effect of subtidal oscillations

320 and baroclinic flows is discussed further in Section 4. In the following, tidal analysis from  
321 model simulations will be compared with observations within the estuary obtained in different  
322 experiments at different time periods (tidal constituents are assumed to be the same throughout).  
323 Our model runs focus on the 35 day period spanning the 2015 field experiment, and will be  
324 compared with observed velocity and sea surface elevation time series from 2015 and tidal  
325 analysis of observations obtained during all experimental periods (Table 1).

326 Time resolution was determined by iteration on grid smoothing and reducing barotropic  
327 and/or baroclinic time steps until numerical stability was achieved. For model simulations  
328 presented herein, a baroclinic time step of 1.5 *s* was used, with barotropic time step 1/20 of that  
329 value. Computations were performed on a Cray XE6m-200 supercomputer at the Institute of  
330 Earth, Ocean, and Space at the University of New Hampshire, and the Blue Waters CRAY XE6  
331 supercomputer located at the University of Illinois-Urbana-Champaign. Output over the whole  
332 domain was stored to disk at 30 *min* average model time intervals, and for 15 *min* averaged  
333 intervals at specific save points corresponding to instrument locations and along a densely  
334 sampled line every 100 *m* along the main transect passing through the entire estuary.

#### 335 **2.4 Model Validation Methods**

336 Model validation is accomplished in four ways. The first is by conducting a tidal  
337 analysis, and comparing the modeled energy decay and phase shift of the dominant M2 tidal  
338 constituent throughout the estuary with similar analysis of observations of sea surface elevation  
339 time series. The second is by comparing modeled time series of the vertical variation in currents  
340 with observations. The third is with cross-spectral analysis between modeled and observed sea  
341 surface elevation, and horizontal velocity components at single locations, and with the evolution  
342 of cross-spectral phase at the M2 frequency between sea surface elevation and along-channel

343 velocities. The fourth is by comparing the growth and phase change of M4 and M6 tidal  
344 harmonic constituents between modeled and observed time series, and by comparison of the  
345 along-estuary evolution of sea surface elevation skewness and asymmetry.

#### 346 **2.4.1 Tidal dissipation and phase change**

347 As the tide propagates into shallow coastal regions and interacts with bottom topography  
348 and basin geometry, it loses energy through frictional processes that result in tidal amplitude  
349 decay and phase changes relative to the open ocean value. Due to phasing of the tide a direct  
350 time series comparison is only possible for model runs that coincide with the specific phases of  
351 the tide during that particular field study. However, tidal analysis of long (30+ day) time series  
352 of sea surface elevation obtained at other times can be compared with non-synchronous model  
353 simulations, provided there are no other atmospheric effects that nonlinearly interact with the  
354 tide and do not substantially change the tidal behavior. Therefore, we conduct a tidal analysis  
355 (using T\_TIDE; Pawlowicz, *et al.*, 2002) to decompose each time series of sea surface elevation  
356 into tidal components and compare the modeled and observed tidal constituent energy from the  
357 linear gravity wave relation,

$$358 \quad E = \frac{1}{2} \rho g A^2 \quad (4)$$

359 where  $E$  is the total energy per unit surface area,  $A$  is the amplitude of the tidal constituent, and  
360 the density  $\rho$  is assumed constant throughout the estuary. In this study the semidiurnal M2 tide  
361 dominates, contributing about 88% of the total tidal energy at the mouth of the estuary. The  
362 energy at any location within the estuary,  $E_{station}$ , is normalized by the value at the estuary  
363 mouth,  $E_{ocean}$ , to represent the fractional energy loss,  $E_{norm}$ , as the tide progresses upstream,

$$364 \quad E_{norm} = (A_{station}/A_{ocean})^2 \quad (5)$$



365 Assuming the uncertainties in the tidal amplitudes,  $\delta A_{station}$  and  $\delta A_{ocean}$ , are both independent and  
366 random, then the error  $\delta E_{norm}$  is calculated following Taylor (1982),

$$367 \quad \delta E_{norm} = E_{norm} \cdot \sqrt{2 * (\delta A_{station}/A_{station})^2 + 2 * (\delta A_{ocean}/A_{ocean})^2} . \quad (6)$$

368 Initial model calibration involves testing different bottom boundary conditions, and iterating to  
369 estimate the energy decay as a function of distance from the estuary mouth that best fits the  
370 observations.

#### 371 **2.4.2 Time series comparison of vertically varying currents**

372 Modeled currents are computed at defined  $\sigma$  coordinate levels that range from  $\sigma = -1$  at  
373 the bottom to  $\sigma = 0$  at the surface. The total water depth in the model is given by the elevation  
374 of the seabed (relative to the model datum defined) plus the corresponding (fluctuating) sea  
375 surface elevation. The observations, on the other hand, are obtained from fixed, upward looking  
376 ADCP's with vertical bin elevations defined in a fixed coordinate system relative to the bottom.  
377 The range over which the currents are observed depends on the instrument characteristics (*e.g.*,  
378 acoustic frequency and instrument capabilities) and the height of the fluctuating sea surface  
379 relative to the bottom. Acoustic interference by side-lobes at the surface limit the range of  
380 useable vertical bins to be less than 94% of the total instantaneous water depth (and appropriate  
381 filtering methods must be employed to eliminate spurious velocities near the surface). As a  
382 consequence, the velocities observed with ADCP's in the field further from the bottom have bins  
383 coming into and out of the water column as the tide rises and falls.

384 To compare the modeled to observed currents, the modeled currents (in  $\sigma$  coordinates)  
385 are transformed to the observational coordinate system by linear interpolation over the  
386 instantaneous water level at each time step. In this manner, the modeled time series at the

387 transformed upper bins also come into and out of the water surface similar to the observations.  
388 Care must also be taken to represent the velocities from the observations at the center of the  
389 vertical bins, and the model at the defined location by the  $\sigma$  coordinates. A representative  
390 example of the time series comparison is shown later (Figure 6) and described in Section 3.2.

### 391 **2.4.3 Cross-spectral Analysis**

392 A more complete evaluation that includes the overall behavior of the modeled velocities  
393 can better be done with cross-spectral analysis that shows the energy density levels for both the  
394 model and the data as a function of frequency, and the coherence and phase relationship for each  
395 frequency. As our interests lie with the tidal constituents, the frequency resolution of the spectra  
396 will necessarily need to be fine enough to resolve the major constituents, with lowest tidal  
397 constituent (the O1 diurnal variation) of about  $0.0417 \text{ hr}^{-1}$ . At the same time, the confidence  
398 intervals on the spectra, coherence, and phase must be high enough to make reasonable  
399 comparisons. For the 30 day time series examined, cross-spectra were computed with 10 degrees  
400 of freedom (DOF) by averaging 5 adjacent frequency bands. The frequency bandwidth of the  
401 smoothed spectral estimates was  $0.0069 \text{ hr}^{-1}$  with lowest resolved frequency of  $0.0035 \text{ hr}^{-1}$ . The  
402 95% confidence intervals are computed for the spectral amplitudes, coherences, and phase. Only  
403 those phase estimates for frequencies with coherence greater than the 95% critical value (0.52 for  
404 10 DOF) are shown (phase error bars for incoherent frequencies are meaningless; Bendat and  
405 Piersol, 2000). To reduce leakage effects, a Hanning data window is applied to each mean-  
406 corrected time series before computing the spectra.

### 407 **2.4.4 Sea surface elevation and along-channel velocity phase difference**

408 Tidal analysis of the sea surface elevation and velocities can be compared to show the  
409 relative change in phase as the tide evolves up the estuary. In this case, the observed and

410 modeled bi-directional velocities were rotated to align with the along-channel direction using  
411 standard rotary analysis (Gonella, 1972). Ellipse orientations for the dominant M2 tidal  
412 frequency defines the angle of the major axis of the rotary ellipse that is used in the rotation to  
413 along-channel direction. We conduct a tidal analysis to decompose each time series of the along-  
414 channel velocity into amplitudes and phases for each harmonic tidal constituent frequency  
415 following the same procedure for the sea surface elevation (see Section 2.4.1). The phase  
416 difference between the sea surface height ( $P$ ) and along-channel velocity ( $U$ ) at the M2 tidal  
417 frequency was computed for time series at locations that span the estuary and reported as the  $P$ -  
418  $U$  phase.

419         The evolution of the  $P$ - $U$  phase for the dominant M2 tidal constituent indicates the nature  
420 of the tidal motion throughout the estuary (Figure 10; top panel). In a progressive wave, the  
421 maximum currents occur at the same time as the maximum height of the wave, and the currents  
422 and amplitude are in phase. In a standing wave the maximum currents occur at mid-tide, half  
423 way between the crest and the trough of the wave, and the along-channel currents are 90 *deg* out  
424 of phase with the sea surface height.

#### 425 **2.4.4 Tidal harmonic growth and phase difference**

426         The growth of the M4 harmonic relative to the M2 constituent is a measure of the  
427 asymmetry and non-linear distortion of the tide (Friedrichs and Aubrey, 1988). Following Speer  
428 and Aubrey (1985), the amplitude ratio,  $A_{ratio}$ , and the phase difference,  $\theta_{diff}$ , is defined as,

$$429 \quad A_{ratio} = A_{M4} / A_{M2} \quad (7)$$

$$430 \quad \theta_{diff} = 2 * \theta_{M2} - \theta_{M4} \quad (8)$$

431 where  $A_{M4}$  and  $A_{M2}$  are the amplitudes of the M4 and M2 tidal constituents, respectively, and

432  $\theta_{M4}$  and  $\theta_{M2}$  represent corresponding phase relationships. In general, stronger frictional effects  
 433 produce larger  $A_{ratio}$ , and the corresponding  $\theta_{diff}$  describes the gross behavior of the tides with  
 434 phase differences between  $0^\circ$  and  $180^\circ$  ( $180^\circ$  and  $360^\circ$ ) indicating flood (ebb) dominance  
 435 (Friedrichs and Aubrey, 1988). Flood dominant systems have characteristically stronger flood  
 436 currents and longer falling than rising tides, whereas ebb dominant systems have stronger ebb  
 437 currents and longer rising tides.

438 The amplitudes and phases of the M2 and M4 tidal constituents are estimated with a tidal  
 439 harmonic analysis (using T\_TIDE) that fits harmonics to the time series and computes error bars  
 440 on the estimates of amplitude and phases for each constituent, allowing estimates of the  
 441 uncertainty in  $A_{ratio}$  and  $\theta_{diff}$  (Taylor, 1982). The error estimates for  $\delta A_{ratio}$  and  $\delta \theta_{diff}$  are  
 442 calculated using the following formulations,

$$443 \quad \delta A_{ratio} = \delta A_{ratio} \cdot \sqrt{(\delta A_{M4}/A_{M4})^2 + (\delta A_{M2}/A_{M2})^2} \quad (9)$$

$$444 \quad \delta \theta_{diff} = \sqrt{(\delta \theta_{M2})^2 + (\delta \theta_{M4})^2} \quad (10)$$

445 following Taylor (1982), similar to  $\delta E_{norm}$  (Equation 6).

446 The third moments, skewness and asymmetry, of observed and modeled sea surface  
 447 elevation time series are computed along the estuary (following Elgar and Guza, 1985). The  
 448 normalized (by the variance to the 3/2 power) skewness describes the general nonlinear deviation  
 449 of the wave profile from a sinusoidal shape to a peaked-up waveform symmetrical about the  
 450 vertical axis through the wave crest. The normalized asymmetry describes the asymmetry about  
 451 the vertical axis, and can indicate a pitched forward (or pitched backwards) wave form. The  
 452 nature of the skewness and asymmetry is determined by the phase relationship between the  
 453 primary frequency and the coupled harmonics. For purely skewed (peaked up, Stokes-like) wave

454 profiles, the asymmetry is zero and the primary and higher harmonics are in-phase. For pitched  
455 forward (backward) the asymmetry is nonzero and negative (positive). Sawtooth profiles have  
456 high negative asymmetries and phase relationships between the primary and first harmonic up to  
457 +/- 90 deg. Evaluation of waveforms for wind-driven surface gravity waves in the ocean and  
458 their relationship to third moments can be found in Elgar and Guza (1985).

### 459 **3. Results: Model-Observation Comparison**

460 Results comparing model simulations for barotropic tides with observations are presented  
461 here, and follow the methodologies discussed previously. Station data are retained from the  
462 model simulations at all the sensor locations, as well as from locations separated by 100 m along  
463 a transect down the main channel extending from the first sensor location outside the mouth of  
464 the estuary to the upper reaches of the Great Bay by the Squamscott River.

#### 465 **3.1 Tidal dissipation and phase change**

466 The observed energy decay and phase change of the M2 tidal constituent relative to the  
467 value at the most seaward location along the station transect through the estuary is shown in  
468 Figure 5. The most seaward observation (1 km from the Ft. Point tidal station) closely matches  
469 the predicted tidal amplitude from the OTPS model, and used to normalize the energy ( $E_{norm}$ ,  
470 Eq. 5). Also shown is the variation in the center channel water depth along the transect. Error  
471 bars (Eq 5-6) on the energy and phase estimates are based on the T\_TIDE analysis. Observations  
472 show an increase in tidal energy near the mouth, and then a progressive decrease in energy  
473 through the energetic, narrow portion of the lower Piscataqua River. This decay is strong (and  
474 somewhat variable) between Portsmouth and Dover Pt., and in general agreement with estimates  
475 of dissipation found by Swift and Brown (1983). By the time the tides reach the Little Bay  
476 entrance, 45% of the M2 tidal energy has been lost. Over this same reach, the M2 phase has

477 changed 50 *deg*, significantly larger than for a simple progressive tidal wave propagating  
478 upstream (with estimate of about 6 *deg* phase change based on shallow water wave phase speeds  
479 and average water depth of 20 *m*), and much less than a standing wave with 90 *deg* phase  
480 change.

481 Interestingly, the tidal amplitudes increase slightly between the entrance to the Little Bay  
482 (Dover Pt.) and the upper reaches of the Great Bay (Squamscott Bridge), indicating some  
483 amplification as the tide propagates into progressively shallower water. Additionally, the phase  
484 continues to evolve (approaching 70 *deg*) suggesting that the tide here is more reflective. It  
485 should be noted that the tidal extent during the flood does not end at the Squamscott Bridge, but  
486 continues an additional 8 *km* inland (as well as up the other rivers; Figure 1).

487 Also shown in Figure 5 are model predictions of the M2 tidal decay and phase change for  
488 a range of apparent bottom roughness,  $z_{ob}$ , from 0.015 – 0.030 *m*. The best fit to the observation  
489 is for  $z_{ob} = 0.02$  *m*. The model increase in M2 energy across the shallowing Great Bay  
490 bathymetry is in general agreement with the observations. In general, the model well predicts the  
491 evolution of the tidal phase throughout the estuary.

### 492 **3.2 Time series comparison of vertically varying currents**

493 Comparisons of modeled and observed current time series (for 4 days) from a single  
494 location in water depth of about 5.75 *m* in the Great Bay is shown in Figure 6. Both the east-  
495 west and north-south velocity comparisons are shown for elevations (relative to MSL) near the  
496 bottom (-4.13 *m*), mid water column (-2.63 *m*), and near the surface (-1.13 *m*). In general, the  
497 modeled velocities closely follow the observations including in the upper water column where the  
498 “sensor” bins are coming into and out of the water as the tide rises and falls. Root-mean-square  
499 (RMS) errors between modeled and observed time series at all elevations above the bottom range

500 0.035-0.049 *m/s* and 0.047-0.055 *m/s* for the east-west and north-south velocity components and  
501 0.095 *m* for sea surface elevation (each about 10% of the amplitude at that location). In general,  
502 the 10% RMS error between model-data time series for all sensors across the Great Bay from the  
503 2015 deployment is quite good, with average RMS errors for sea surface elevations, east-west,  
504 and north-south velocities of 0.096 *m*, 0.054 *m/s*, and 0.060 *m/s*, respectively.

### 505 **3.3 Cross-spectral Analysis**

506 Cross-spectra between modeled and observed sea surface elevation, east-west, and north-  
507 south currents from a location in the Great Bay are shown in Figure 7. Modeled and observed  
508 spectral density,  $F$ , show similar energy distribution at the tidal constituents, and compare well  
509 for the sea surface elevation and both orthogonal components of the velocity. Note that the noise  
510 floor associated with the observed spectra is much higher than for the model, a result owing to  
511 the sampling uncertainty associated with the pressure sensors and acoustic profiling instruments,  
512 as well as the model not considering baroclinic flows (discussed later).

513 The coherence squared,  $\gamma^2$ , is high (0.99) at the tidal harmonic frequencies, well above  
514 the critical value (0.52). The corresponding phase at the energetic M2 frequency is 2.47 *deg* for  
515 the sea surface elevation time series, and 8.48 and 3.98 *deg* for the east-west and north-south  
516 velocities, respectively. The average model-data phase at the M2 frequency for all sensors in the  
517 Great Bay during the 2015 deployment for sea surface elevation and the bi-directional velocities  
518 was 0.03, 0.34, and 2.32 *deg*, respectively.

### 519 **3.4 Tidal harmonic growth and phase difference**

520 Modeled and observed power spectra of sea surface elevation,  $F$ , from two locations  
521 spanning the estuary – one near the mouth at Fort Point and the other in the Great Bay – are

522 shown in Figure 8. The M2 tidal energy decays by about 45% (as shown in Figure 5). On the  
523 other hand, the spectra show a sharp increase in the energy levels at the tidal harmonics in the  
524 Great Bay, evident well beyond the M4 and M6 constituents indicating the strong growth of  
525 overtides and nonlinear evolution of the spectra. The growth of the M6 harmonic exceeds that of  
526 the M4 harmonic, consistent between the modeled and observed spectra.

527 To examine the spatial nonlinear evolution of the tidal spectra, the M2, M4, and M6 tidal  
528 constituents (as determined by T\_TIDE analysis) along the center channel from the mouth to the  
529 upper reaches of the Great Bay is shown in Figure 9 (along with the depth variation along the  
530 transect). The M2 tidal amplitude decays as expected. Modeled M4 and M6 harmonics increase  
531 from 2% to 7% of the M2 amplitude, consistent with the observations. Interestingly, the M4  
532 amplitude first grows through the first 8 km of the Piscataqua River, then decays to very small  
533 value at Dover Pt., and then grows again in the upper reaches (last 3 km) of the Great Bay over  
534 the mudflats. The spatial evolution of the M4 tidal constituent is qualitatively similar to the  
535 observations but underestimates the magnitude by about a factor of 2 in the narrows of the lower  
536 Piscataqua River, and overestimates in the upper reaches of the Great Bay. Similar results are  
537 obtained if we include baroclinic or subtidal flows. We do not fully understand why this is  
538 occurring, but may arise from complexities in the bathymetry and sidewalls in this part of the  
539 estuary not well resolved in the model, or from viscous or turbulent effects assumed constant  
540 throughout the model domain. Moreover, it has been shown that locally high values of the M4  
541 tide can occur near headlands as a result of the centrifugal component of the advection of M2  
542 momentum (Parker 1984). Further investigation will need to address the role of bathymetric  
543 resolution and topography in the local generation of the M4 tide. The M6 tidal amplitude shows  
544 a steady increase throughout the estuary, leveling off (and even decaying near the Squamscott)



545 over the final 3 km in the Great Bay. The M6 tidal constituent, driven primarily by frictional  
546 effects (Parker, 1991), appears to be well modeled throughout the estuary.

547 The phase evolution across the estuary is shown in Figure 10 (top panel) for the M2 tidal  
548 frequency at all observation stations where time series are available (Table 1). The modeled  
549 evolution of the  $P-U$  phase closely follows that of the observations. The  $P-U$  phase relationship  
550 in the first 12 km of the estuary is consistently about 45 degrees indicating a partially progressive  
551 and standing wave motion. However, 12 km upstream the  $P-U$  phase abruptly changes to +90  
552 deg, consistent with a standing wave from Dover Pt. through the Great Bay Estuary. This  
553 change in  $P-U$  relationship is consistent with the observed tidal dissipation and relative phase  
554 change of the M2 tidal constituent (Figure 5).

555 Also shown in Figure 10 is the evolution of the growth of the M4 relative to the M2  
556 constituent ( $A_{ratio}$ ; Equation 7). The modeled growth of the M4 harmonic increases through the  
557 first half of the lower Piscataqua River, decreasing at Dover Pt., and then increasing again  
558 through the upper reaches of the Great Bay (to about 8% of the M2 amplitude) where the depth  
559 shallows significantly over the mudflats. The evolution of the tide depends strongly on the water  
560 depth, consistent with a nonlinearly shoaling tidal wave. This spatial behavior is qualitatively  
561 consistent with the observations that show about twice as much harmonic growth as the model in  
562 the lower Piscataqua.

563 Also shown in Figure 10 is  $\theta_{diff}$  (Equation 8), an indication of the relative importance of  
564 the ebb and flood tide to the circulation (following Friedrichs and Aubrey, 1988). Although the  
565 model under-predicts the growth of the M4 constituent, the phase differential is qualitatively  
566 consistent with the observations. The lower reaches of the estuary in the Piscataqua River show  
567 ebb dominance, consistent with a stronger receding tide as the estuary drains. The Great Bay

568 (beyond Adam's Pt.), on the other hand, shows a strong flood dominance, indicating the flows  
569 into the bay and over the mudflats are greater than that produced by the ebb tide. This behavior  
570 is consistent with the evolution of the sea surface elevation skewness and asymmetry (Figure  
571 10). The skewness shows similar trend to  $A_{ratio}$  and  $\theta_{diff}$ , and is relatively low through the  
572 Piscataqua river, growing in the Little Bay and Great Bay suggesting a strong nonlinear  
573 evolution to the shoaling tide wave with asymmetrical form about the horizontal (along-channel)  
574 axis. The asymmetry increases in magnitude sharply in the Great Bay, indicating a pitched  
575 forward wave profile that has shorter duration but stronger flood currents and longer duration but  
576 weaker ebb currents, consistent with the flood dominance estimated from  $\theta_{diff}$ .

#### 577 **4. Discussion**

578 The tidal dissipation and phase evolution in the model is modified by the choice of  
579 apparent bottom roughness,  $z_{ob}$ . A range of values for  $z_{ob}$  were introduced in model simulations  
580 and the best fit of the model tidal analysis to the observed M2 energy and phase evolution used  
581 to determine the most appropriate value. Our best estimate,  $z_{ob} = 0.02 m$ , is consistent with  
582 Swift and Brown's (1983) estimates based on the 1975 observations. In their work, they find a  
583 range of frictional coefficients from 0.015 to 0.054. They also note that the dissipation was  
584 highest in regions where the flows were larger, generally occurring in parts of the estuary where  
585 there are constrictions in the flow owing to a narrowing of the river channel. Our model results  
586 show that ranges of  $z_{ob}$  from 0.015 to 0.030  $m$  give reasonable results throughout the estuary,  
587 and suggest that the dissipation is well represented with a single value. This is somewhat  
588 surprising in that the character of the seafloor (ranging from rocky and coarse sediments in the  
589 channels to fine sands and muds on the flats) changes significantly over the estuary. On the  
590 other hand, the flows also change similarly. That is, where the flows are highest, the more rocky

591 the bottom and more coarse the sediments (*i.e.*, the fine material is washed away), and where the  
592 flows are weak, the more fine-grained the sediments and the nature of the bottom changes (*i.e.*,  
593 with tidal channels cut through the mud and vegetation).

594 Model simulations that include and exclude subtidal forcing show that the tidal  
595 dissipation (based on tidal analysis and considering only the M2 tidal constituent) does not  
596 change significantly (Figure 11). This suggests that for the conditions examined with subtidal  
597 amplitudes ranging 0.10-0.30 *m* over the 30-day model runs and observation periods, the  
598 nonlinear interaction with the tides is weak. This also suggests that tidal dissipation and phase  
599 change produced from the model simulations conducted with 2015 forcing conditions can be  
600 compared with observations taken at other times (for example, from all the other experiments;  
601 Table 1).

602 The freshwater input to the Great Bay estuarine system is relatively small and during  
603 non-storm conditions contributes about 2% of the tidal prism (Short, 1992; NHDES, 2007).  
604 Baroclinic model simulations with average river discharge and average salinity and temperatures  
605 had a negligible effect on the tidal constituent amplitudes and phases, and can generally be  
606 ignored for the Great Bay when considering the tidal dynamics. However, comparisons of  
607 modeled time series and spectra with observations suggest that baroclinic flows are present.  
608 RMS velocity comparisons between barotropic and baroclinic model simulations away from the  
609 rivers but within the Great Bay are quite similar, and agree to within about 0.01-0.02 *m/s*.  
610 However, in the deep channel of the Little Bay where the flow field is high and has strong lateral  
611 shear, the baroclinic model velocities deviate from the barotropic velocities by about 0.05-0.10  
612 *m/s*. Moreover, spectral comparisons show that, although the energetic tidal frequencies are not  
613 strongly affected, the high frequencies and the noise floor between the tidal harmonics increases

614 for the baroclinic flows. This suggests that if higher frequency flows are of interest, then  
615 baroclinic models should be considered, but that tidal dynamics are well modeled with barotropic  
616 approximations.

617 In this work, we have not considered the effects of waves or winds on the tidal circulation  
618 and dissipation. In hindsight, this appears to be a reasonable assumption, at least for the  
619 conditions that occurred during the various field experiments. As noted by Wengrove, *et al.*  
620 (2015), wind-generated currents during a large storm can enhance the tidal flows when the winds  
621 are in the same direction as the current. Considering that the tides reverse every 12.4 *hr* in the  
622 Great Bay, this direct wind-driven flow might have an asymmetric effect on the overall current  
623 speeds and directions, sometimes in the direction of the flow and other times opposing or acting  
624 at an angle. In any case, the effect appears to be small even for the large wind event examined in  
625 Wengrove, *et al.* (2015), and does not likely change the overall character of the tidal currents  
626 owing to the order of magnitude difference between the wind-induced flows (of order 0.1 *m/s*)  
627 and the tides (of order 1- 2 *m/s*). This may not be true closer to shore where the tidal flows are  
628 weaker and the wind-induced currents may be proportionally larger.

629 The model-data comparisons show that the ROMS model reasonably well simulates the  
630 tidal dissipation and nonlinear evolution throughout the Great Bay Estuarine system. Ignoring  
631 baroclinic flow and subtidal oscillations does not strongly affect the tidal dynamics, at least for  
632 typical non-storm conditions for the Great Bay region. The model makes the hydrostatic  
633 approximation, and solves the RANS equations in three-dimensions following rectilinear  
634 horizontal grid and a vertical terrain-following  $\sigma$  coordinate system. Many other models (such  
635 as ADCIRC, Westerink, *et al.*, 1992; FVCOM, Chen, *et al.*, 2003; Delft3D, Lesser, *et al.*, 2004)  
636 also solve the same equations with similar approximations for rectilinear or unstructured grids

637 and would likely also produce similar results. The good agreement between modeled and  
638 observed velocities across the estuary tidal channels and over the mud flats suggests that  
639 modeled currents from these fully nonlinear models would produce a good representation of the  
640 flow fields useful for sediment transport and nutrient flux studies (the subject of ongoing work).

## 641 **5. Conclusions**

642 A high-resolution three-dimensional hydrodynamic model (ROMS) was implemented for  
643 the Piscataqua River - Great Bay estuary using observed bathymetry and validated with several  
644 observational datasets spanning the estuary. The model was able to reproduce the observed tidal  
645 dissipation characteristics including dominant semidiurnal M2 tidal amplitude decay and phase  
646 changes, as well as the nonlinear growth of the M4 and M6 harmonics. The model  
647 underestimates the spatial evolution of the M4 magnitude by about a factor of 2 in the narrows of  
648 the lower Piscataqua River, and overestimates the values in the upper reaches of the Great Bay  
649 toward the Squamscott River. This could be due to complexities in the bathymetry and sidewalls  
650 in this part of the estuary not considered in the model, or from viscous or turbulent effects  
651 assumed constant throughout the model domain, and should be the topic of further investigation.  
652 The modeled behavior reproduces a highly dissipative, partially progressive wave in the lower 12  
653 km of the Piscataqua River (with 45% tidal energy loss by Dover Pt., consistent with previous  
654 observational studies; Swift and Brown, 1983), and a (nearly) standing wave in the low  
655 dissipative region between Dover Pt. and the upper reaches of the Great Bay. The spatial  
656 evolution from the mouth upstream in the estuary of the tidal harmonics, sea surface elevation  
657 skewness and asymmetry, and phase relationship between the along-channel velocity and sea  
658 surface time series, indicates a strong nonlinear tidal evolution consistent with an ebb dominant  
659 flow in the lower Piscataqua, and a flood dominant flow in the Great Bay. The good

660 comparisons with observations suggest that the model well represents the nonlinear behavior of  
661 the tide, and accurately simulates the velocity and sea surface elevation time series throughout  
662 the estuary. Differences between model simulations with and without subtidal oscillations or  
663 river fluxes for the Great Bay are small, suggesting that interactions between the tide and other  
664 low frequency (subtidal) or baroclinic flows are weak and can be ignored when considering tidal  
665 dynamics.

## 666 **Acknowledgement**

667 Funding for this work was supported by the Office of Naval Research (ONR) Littoral  
668 Geosciences and Optics Program under grant number N00014-14-1-0557, New Hampshire Sea  
669 Grant Project R/HCE-1 under grant number NA14OAR4170083, and with funds provided by the  
670 University of New Hampshire. This research is part of the Blue Waters sustained-petascale  
671 computing project, which is supported by the National Science Foundation (awards OCI-  
672 0725070 and ACI-1238993) and the state of Illinois. Blue Waters is a joint effort of the  
673 University of Illinois at Urbana-Champaign and its National Center for Supercomputing  
674 Applications. Computations were also performed on Trillian, a Cray XE6m-200 supercomputer  
675 at the Institute for Earth, Ocean, and Space at UNH supported by NSF MRI program under grant  
676 PHY-1229408. Jon Hunt provided field assistance for the 2015 field experiments. The 2007  
677 observations were obtained by Karl Kammerer of NOAA. Chris Sherwood of the USGS and  
678 Jamie Pringle of UNH assisted with establishing a stable model for the simulations presented.

## 679 **References**

680 Armstrong, P.B., Hanson, G.M., and Gaudette, H.E., 1976. Minor elements in sediments of Great  
681 Bay Estuary, New Hampshire, *Env. Geology*. 1, 207-214.

682 Aubrey, D., and Speer, P.E., 1985. A study of Non-linear tidal propagation in  
683 shallow Inlet/Estuarine Systems. Part I : Observations. *Estuarine, Coastal and Shelf*  
684 *Science*. 21, 185-205.

685 Bendat, J.S., and Piersol, A.G., 2000. Random data: analysis and measurement procedures, 3<sup>rd</sup>  
686 Edition, Wiley-Interscience, New York, 566 pp.

687 Boon, J. D., and Byrne, R.J., 1981. On basin hypsometry and the morphodynamic response of  
688 coastal inlet systems. *Mar. Geol.* 40 (1-2), 27-48.

689 Brown, W.S., and Irish, J.D., 1992. The Annual evolution of geostrophic flow in the Gulf of  
690 Maine: 1986-1987, *J. Phys. Oceanogr.* 22, 445-473.

691 Brown, W.S., and Trask, R.P., 1980. A study of tidal energy dissipation and bottom stress in an  
692 estuary. *J. Phys. Oceanogr.* 10, 1742-1754.

693 Carter, G.S. and Merrifield, M.A, 2007. Open boundary conditions for regional simulations.  
694 *Ocean Modelling*. 18, 194-209.

695 Chapman, D.C., 1985. Numerical treatment of cross-shelf open boundaries in a barotropic  
696 coastal ocean model. *J. of Phys. Oceanogr.* 15, 1060-1075.

697 Chen, C., Liu, H., and Beardsley, R.C., 2003. An Unstructured Grid, Finite-Volume, Three-  
698 Dimensional, Primitive Equations Ocean Model: Application to Coastal Ocean and  
699 Estuaries. *J. Atmos. Ocean. Tech.* 20, 159–186.

700 Dronkers, J., 1986. Tidal Asymmetry and Estuarine Morphology. *Netherlands Journal of Sea*  
701 *Research*. 20 (2/3),117-131.

702 Egbert, G.D., and Erofeeva, S.Y., 2002. Efficient inverse modeling of barotropic ocean tides. *J.*  
703 *Ocean. Atmos. Tech.* 19, 183-204.

704 Elgar, S., and Guza, R.T., 1985. Observations of bispectra of shoaling surface gravity waves, *J.*  
705 *Fluid Mech.* 161, 425-448.

706 Erturk, S.N., Bilgili, A., Swift, M.R., Brown, W.S., and Celikkol, B., 2002. Simulation of the  
707 Great Bay Estuarine System: Tides with tidal flats wetting and drying. *J. Geophys. Res.*  
708 107 (C5), 3038. <https://doi.org/10.1029/2001JC000883>

709 Flather, R.A., 1976. A tidal model of the northwest European continental shelf. *Memoires de la*  
710 *Societe Royale de Sciences de Liege.* 6, 141-164.

711 Friedrichs, C., and Aubrey, D., 1988. Non-linear tidal distortion in shallow well-mixed estuaries:  
712 a synthesis. *Estuarine, Coastal and Shelf Science.* 27, 521-545.

713 Garrett, C., 1972. Tidal resonance in the Bay of Fundy and Gulf of Maine. *Nature.* 238, 441-443.

714 Geyer, W.R., and MacCready, P., 2014. The estuarine circulation, *Annual Review of Fluid Mech.*  
715 46. 175-197.

716 Gonella, J., 1972. A rotary-component method for analyzing meteorological and oceanographic  
717 vector time series. *Deep-Sea Research.* 19, 833-846.

718 Haidvogel, D.B., Arango, H., Budgell, W.P., Cornuelle, B.D., Curchitser, E., Di Lorenzo, E.,  
719 Fennel, K., Geyer, W.R., Hermann, A.J., Lanerolle, L., Levin, J., McWilliams, J.C.,  
720 Miller, A.J., Moore, A.M., Powell, T.M., Shchepetkin, A.F., Sherwood, C.R., Signell,  
721 R.P., Warner, J.C., and Wilkin, J., 2008. Ocean forecasting in terrain-following  
722 coordinates: formulation and skill assessment of the Regional Ocean Modeling System. *J.*  
723 *Comp. Physics.* 227, 3595–3624.

724 Ip, J.T.C., Lynch, D.R., Friedrichs, C.T., 1998. Simulation of estuarine flooding and dewatering,  
725 with application to Great Bay, NH. *Estuarine and Coastal Shelf Science.* 47, 119-141.



726 Kantha, L.H., and Clayson, C.A., 1994. An improved mixed layer model for geophysical  
727 applications, *J. Geophys. Res.* 99, 25,235–25,266.

728 Kundu, P.K., 1990. Fluid Mechanics, Academic Press, San Diego, 155.

729 Lesser, G.R., Roelvink, J.A., van Kester, J.A.T.M., and Stelling, G.S., 2004. Development and  
730 validation of a three-dimensional morphological model. *J. Coastal Eng.* 51, 883-915.

731 Lewis, M.J., Neill, S.P., Hashemi, M.R., and Reza, M., 2014. Realistic wave conditions and  
732 their influence on quantifying tidal stream energy resource. *Applied Energy.* 136, 495-  
733 508.

734 Marchesiello, P., McWilliams, J.C., Shchepetkin, A., 2001. Open boundary conditions for long-  
735 term integration of regional oceanic models. *Ocean Modeling.* 3, 1-20.

736 McLaughlin, J.W., Bilgili, A., and Lynch, D.R., 2003. Numerical modeling of tides in the Great  
737 Bay Estuarine System: dynamical balance and spring-neap residual modulation.  
738 *Estuarine, Coastal, and Shelf Science.* 57, 283-296.

739 Moriarty, J.M., Harris, C.K., Hadfield, M.G., 2014. A hydrodynamic and sediment transport  
740 model for the Waipoa Shelf, New Zealand: Sensitivity of Fluxes to Spatially-Varying  
741 Erodibility and Model Nesting. *J. Mar. Sci. Eng.* 2, 336-369. doi:10.3390/jmse2020336.

742 Neill, S.P., Hashemi, M.R., and Lewis, M.J., 2014. The role of tidal asymmetry in characterizing  
743 the tidal energy resource of Orkney. *Renewable Energy.* 68, 337-350.

744 NHDES, 2007. New Hampshire Estuaries Project, Hydrologic parameters for New Hampshire's  
745 estuaries. Prepared by P. Trowbridge (Available at [http://www.nhep.unh.edu/resources/  
746 pdf/hydrologic\\_parameters\\_for\\_nhep\\_07.pdf](http://www.nhep.unh.edu/resources/pdf/hydrologic_parameters_for_nhep_07.pdf)).

747 Palma, E.D., and Matano, R.P., 1998. On implementation of passive open boundary conditions

748 for a general circulation model: the barotropic mode. *J. of Geophys Res.* 103, C1, 1319-  
749 1341.

750 Palma, E.D., and Matano, R.P., 2000. On implementation of passive open boundary conditions  
751 for a general circulation model: the three dimensional case. *J. of Geophys Res.* 105, C4,  
752 8605-8627.

753 Parker, B.B., 1984. Frictional Effect on the Tidal Dynamics of a Shallow Estuary. PhD.  
754 Dissertation, The Johns Hopkins University, Baltimore, Maryland, 292 pages.

755 Parker, B.B., 1991. The relative importance of the various non-linear mechanisms in a wide  
756 range of tidal interactions (review). *Tidal Hydrodynamics*. John Wiley, New York. 237-  
757 268.

758 Pawlowicz, R., Beardsley, B., and Lentz, S., 2002. Classical tidal harmonic analysis including  
759 error estimates in MATLAB using T\_TIDE. *Computers and Geosciences*. 28, 929-937.

760 Plant, N.G., Holland, K.T., and Puleo, J.A., 2002. Analysis of the scale of errors in nearshore  
761 bathymetric data. *Marine Geology*. 191, 71-86.

762 Shchepetkin, A.F., and McWilliams, J.C., 2005. The Regional Oceanic Modeling System  
763 (ROMS): A split-explicit, free-surface, topography-following-coordinate oceanic  
764 model. *Ocean Modeling*. 9, 347-404

765 Short, F.T., 1992. The Ecology of the Great Bay Estuary, New Hampshire and Maine: An  
766 Estuarine Profile and Bibliography. NOAA – Coastal Ocean Program Publ. 222 pp.

767 Silver, A.L., and Brown, W.S., 1979. Great Bay estuarine field program 1975 data report Part II;  
768 temperature, salinity and density. University of New Hampshire Sea Grant Technical  
769 Report UNH-SG-167, 42 pp.

770 Speer, P.E., and Aubrey, D., 1985. A study of Non-linear tidal propagation in  
771 shallow Inlet/Estuarine Systems. Part II: Theory. *Estuarine, Coastal and Shelf Science*.  
772 21, 207-224.

773 Swenson, E., Brown, W.S., and Trask, R.P., 1977. Great Bay estuarine field program 1975 data  
774 report Part I: currents and sea levels. University of New Hampshire Sea Grant Technical  
775 Report UNH-SG-157, 109 pp.

776 Swift, M.R., and Brown W.S., 1983. Distribution of bottom stress and tidal energy dissipation in  
777 a well mixed estuary. *Estuarine and Coastal Shelf Science*, 17, 297-317.

778 Taylor, J.R., 1982. An Introduction to Error Analysis: the study of uncertainties in physical  
779 measurements. Mill Valley, Calif: University Science Books.

780 Umlauf, B.H., Burchard, H. 2003. A generic length-scale equation for geophysical turbulence  
781 models. *Journal of Marine Research*. 61, 235-265.

782 Warner, J.C., Geyer, W.R., and Lerczak, J.A., 2005a. Numerical modeling of an estuary: A  
783 comprehensive skill assessment, *J. Geophys. Res.* 110, C05001,  
784 doi:10.1029/2004JC002691

785 Warner, J.C., Sherwood, C., Arango, H., and Signel, R., 2005b. Performance of four turbulence  
786 closure models implemented using a generic length scale method. *Ocean Modeling*. 8,  
787 81-113.

788 Warner, J.C., Sherwood, C.R., Signell, R.P., Harris, C., and Arango, H.G., 2008. Development of  
789 a three dimensional, regional, coupled wave, current, and sediment-transport model.  
790 *Computers and Geosciences*. 34, 1284-1306.

791 Warner, J. C., Armstrong, B., He, R., and Zambone, J. B., 2010. Development of a Coupled

792 Ocean–Atmosphere–Wave–Sediment Transport (COAWST) Modeling System. *Ocean*  
793 *Modeling*. 35, 230-244.

794 Warner, J.C., Defne, Z., Haas, K., and Arango, H., 2013. A wetting and drying scheme for  
795 ROMS. *Computers & Geosciences*. 35, 54-61.

796 Wengrove, M.E., Foster, D.L, Kalnejais, L.H., Percuoco, V., and Lippmann, T.C., 2015. Field  
797 and laboratory observations of bed stress and associated nutrient release in a tidal estuary.  
798 *Estuarine, Coastal and Shelf Science*. 161, 11-24.

799 Westerink, J.J., Luetlich R.A., Baptists A.M., Scheffner N.W. and P. Farrar, 1992. Tide and storm  
800 surge predictions using finite element model. *J. Hydraulic Engng.*, 118 (10), 1373-1390.

801 Yang, Z., Richardson, P., Chen, Y., Kelley, J.G., Myers, E., Aikman III, F., Peng, M., Zhang, A.,  
802 2016. Model development and hindcast simulations of NOAA’s Gulf of Maine  
803 Operational Forecast System. *J. of Mar. Sci. Eng.* 4, 77.

804 Zhang, W.G., Wilkin, J.L., Chant, R.J., 2009. Modeling the pathways and mean dynamics of  
805 river plume dispersal in the New York Bight. *J. Phys. Oceanogr.*, 39, 1167-1183.

**Table 1: Observations used in the study with number of locations and duration of deployments.**

<b>Year – Program</b>	<b>Data Variable</b>	<b>Number of Locations</b>	<b>Duration</b>
1975 – Great Bay Estuary Field Program (Swenson <i>et. al.</i> 1977, Silver and Brown, 1979)	Water Level <sup>a,b</sup>	10*	21 – 333 days
2007 – Piscataqua River Current Survey ( <a href="https://tidesandcurrents.noaa.gov/cdata">https://tidesandcurrents.noaa.gov/cdata</a> )	Water Level and Currents <sup>c,d</sup>	10	41 – 45 days
2009 – CCOM Great Bay Survey	Water Level <sup>e,f</sup>	6	9 – 84 days
2015 – Great Bay Field Study	Water Level and Currents <sup>g,h,i,j</sup>	8+	7 – 35 days
2016 – Great Bay Field Study	Water Level and Currents <sup>d</sup>	1	71 days
NOAA Tide Gauge (8423898) at Ft. Point ( <a href="https://tidesandcurrents.noaa.gov/stationhome.html?id=8423898">https://tidesandcurrents.noaa.gov/stationhome.html?id=8423898</a> )	Water Level <sup>k</sup>	1	Continuous
2009-2016 – UNH Great Bay Buoy ( <a href="http://www.opal.sr.unh.edu/data/buoys/great_bay/index.shtml">http://www.opal.sr.unh.edu/data/buoys/great_bay/index.shtml</a> )	Salinity <sup>l</sup>	1	Seasonal (~ 9 months)

\* Original data unavailable; water levels and current analysis used in this study are provided in Swift and Brown (1983).

+ One instrument was moved to 4 different locations within Great Bay for deployments between 7 and 14 days

a. automatic digital recording (ADR) tide gauge

b. Metritape Inc. Level sensor

c. 600 kHz RDI ADCP

d. 1200 kHz RDI ADCP

e. Aanderaa tide gauge

f. SeaBird Seacat

g. 500 kHz RDI Sentinel V ADCP

h. 1200 kHz RDI Workhorse Sentinel ADCP

i. 3 mHz Sontek Argonaut ADCP

j. 2 mHz Nortek Aquapro ADCP

k. acoustic water level (Next Generation Water Level Measurement System)

l. YSI 6600 Sonde

## List of Figures:

Figure 1. Site location of the Great Bay Estuary and Piscataqua River in southwestern New Hampshire, USA, relative to the Gulf of Maine (inset). The location of the 8 principal rivers of the estuary are indicated, as well as Fort Pt. (the location of a NOAA tide gauge), Dover Pt. (at the entrance to the Little Bay), and Adams Pt. (at the entrance to the Great Bay).

Figure 2. Topographic and bathymetric elevations relative to mean sea level for the Great Bay Estuary. Background image is from Landsat 8.

Figure 3. Observational measurement locations. Along-channel distance from the mouth of the estuary is determined using the PIR0701 sensor (most seaward diamond symbol) from the 2007 NOAA Piscataqua River Current Survey.

Figure 4. Rotated ROMS horizontal grid ( $\xi, \eta$ ) coordinates and model defined boundaries. Displayed gridlines are every 1 km, decimated by a factor of  $33\frac{1}{3}$  from actual model grid (for display purposes). Cardinal directions of boundaries are relative to the orientation of the rotated grid.

Figure 5. M2 tidal energy decay,  $E_{norm}$ , (upper panel) and phase evolution ( $deg$  Greenwich; middle panel) as a function of distance from the mouth of the estuary for different bottom roughness values ( $z_{ob}$ ) of the logarithmic drag law bottom boundary condition. Observations are included as symbols with error bars based on T\_TIDE analysis and following Taylor (1982). Depth profile along the center channel is shown in the lower panel with locations of Fort Point, Dover Point, Adams Point, and the Squamscott River are indicated.

Figure 6. Modeled (dots) and observed (solid line) time series of east-west (left) and north-south (right) velocities from sensor located in 5.75 m water depth in the Great Bay. The vertical elevation relative to mean sea level (in m) of each time series comparison is indicated on the right-hand-side of each panel. The discontinuous time series in the upper three panels are a result of tidal variations in water depth periodically exposing and inundating upper sensor locations near the sea surface. RMS errors range 0.035-0.049 m/s and 0.047-0.055 m/s for the east-west and north-south velocities, respectively.

Figure 7. Cross-spectra between modeled and observed sea surface elevation (left panels), east-west depth-averaged velocity (center panels), and north-south depth-averaged velocity (right panels) for sensor location in 5.75 m water depth in the Great Bay. Upper panels show spectral density,  $F$ , in  $m^2/s$  for sea surface elevation and  $m^2/s$  for velocities as a function of frequency ( $hr^{-1}$ ). Spectra were computed with a Hanning data window and 10 DOF. The 95% confidence interval is shown in the upper center panel. Observed spectra have a significantly higher noise floor but still below the energy levels of the harmonics. Center panels show the coherence squared,  $\gamma^2$ , with 95% significance level as the horizontal dashed line. Lower panels show the phase ( $deg$ ) with solid circles indicating significant phases with 95% confidence intervals.

Figure 8. Modeled (left) and observed (right) spectral density,  $F$  ( $m^2/s$ ), of sea surface elevation from two stations, one near the mouth of the estuary (Fort Point; solid line) and one in 5.75 m

water depth in the Great Bay (dotted line). Spectra show the growth of the tidal harmonics from the ocean to 20 km up the estuary (the M2, M4, and M6 constituents are indicated). Spectra were computed over a 30 day record and processed with a Hanning data window. Observed spectra have a significantly higher noise floor but still below the energy levels of the harmonics.

Figure 9. Modeled (lines) and observed (symbols) amplitude evolution of the M2 (top), M4 (2<sup>nd</sup> from top), and M6 (3<sup>rd</sup> from top) tidal constituents from Fort Point, near the mouth of the estuary, to the Great Bay. Amplitudes were determined with T\_TIDE analysis of 30+ day records (or for the 1975 data from the literature of which no error bars are available). Model results for a range of bottom roughness,  $z_{ob}$ , are indicated in the legend. The depth profile along the center channel is shown in the lower panel.

Figure 10. Modeled (lines) and observed (symbols) along-channel evolution of the  $P-U$  phase ( $deg$ ; top panel),  $A_{ratio}$  (2<sup>nd</sup> from top),  $\theta_{diff}$  (3<sup>rd</sup> from top; showing flood and ebb dominance), normalized skewness (4<sup>th</sup> from top), and normalized asymmetry (5<sup>th</sup> from top) of 30 day sea surface elevation time series from the ocean to the upper reaches of the Great Bay. The nonlinear evolution of the tide is clearly evident with the sea surface profile evolving from a partially progressive nearly sinusoidal form and ebb dominance between Fort Pt. and Dover Pt., to a nearly standing wave with highly skewed and pitched-forward shape and flood dominance in the Great Bay. Model results for a range of bottom roughness,  $z_{ob}$ , are indicated in the legend. The depth profile along the center channel is shown in the lower panel.

Figure 11. Modeled amplitude evolution for tidal only (solid lines) and tidal plus subtidal forcing (symbols) for the M2 tidal constituents from Fort Point, near the mouth of the estuary, to the Great Bay. Amplitudes were determined with T\_TIDE analysis of 30+ day records. Model results for a range of bottom roughness,  $z_{ob}$ , are indicated in the legend. The depth profile along the center channel is shown in the lower panel.

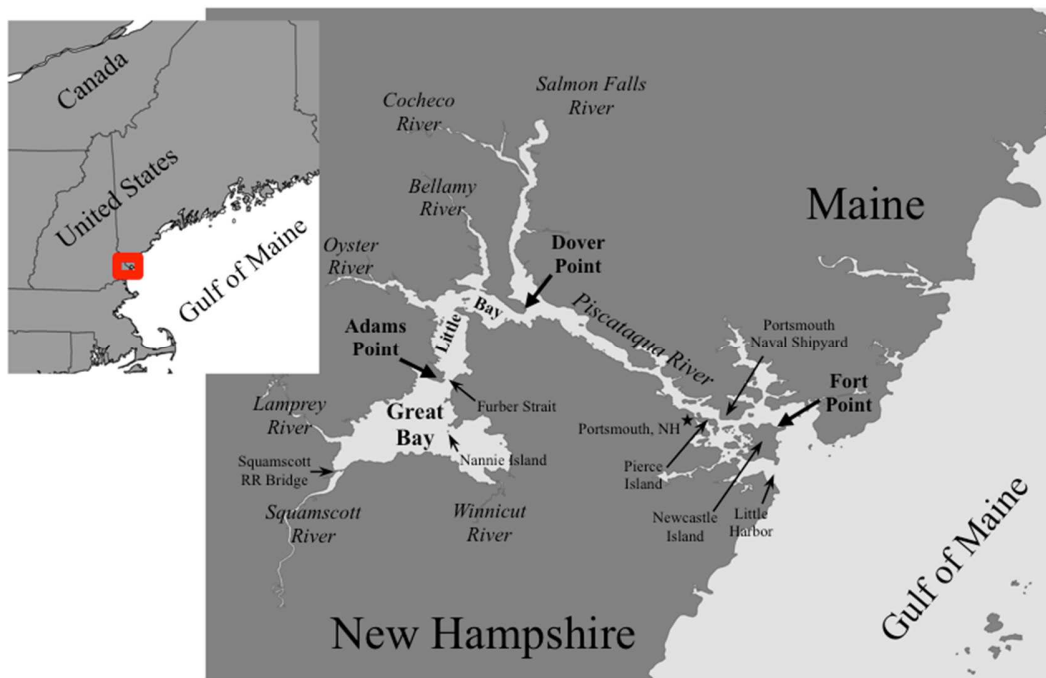


Figure 1: Site location of the Great Bay Estuary and Piscataqua River in southwestern New Hampshire, USA, relative to the Gulf of Maine (inset). The location of the 8 principal rivers of the estuary are indicated, as well as Fort Pt. (the location of a NOAA tide gauge), Dover Pt. (at the entrance to the Little Bay), and Adams Pt. (at the entrance to the Great Bay).



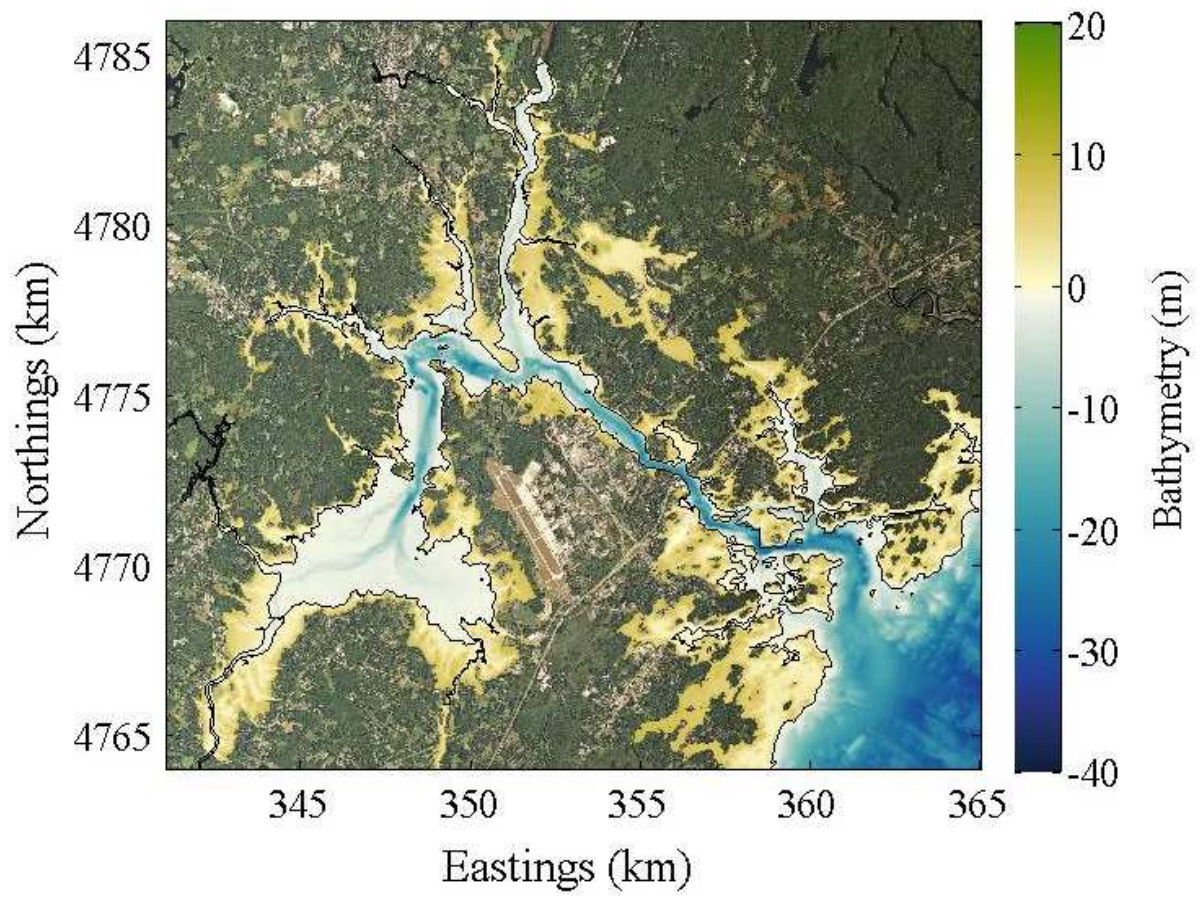


Figure 2: Topographic and bathymetric elevations relative to mean sea level for the Great Bay Estuary. Background image is from Landsat 8.

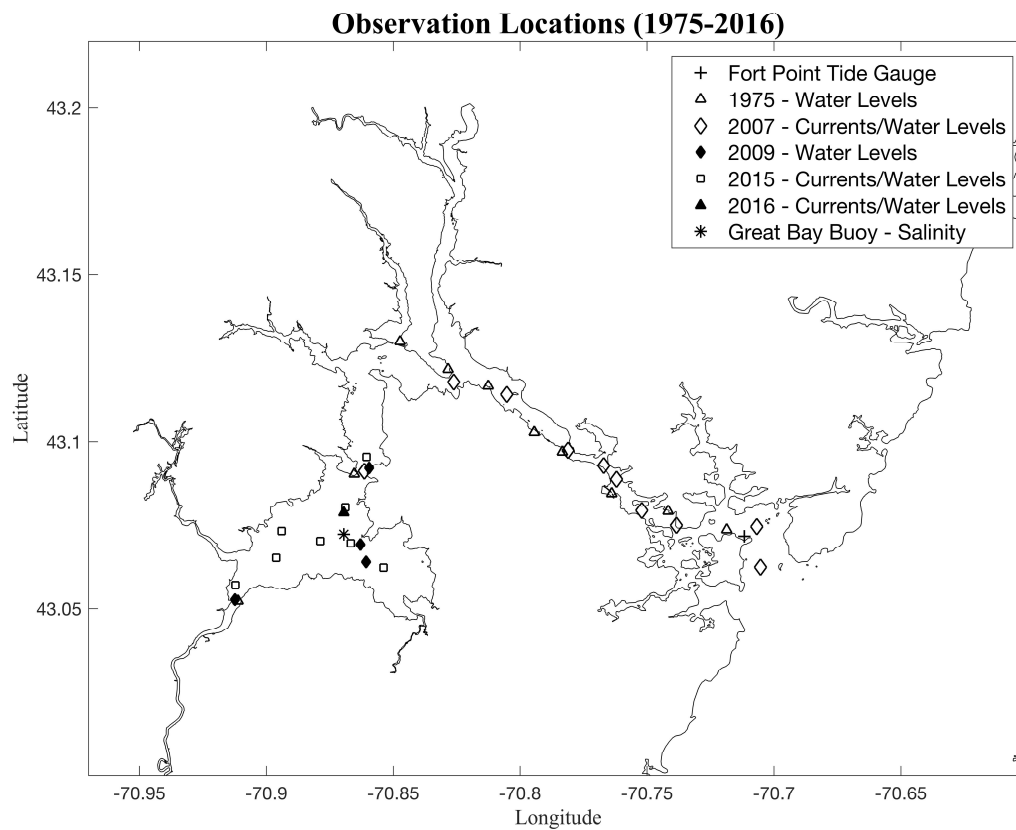


Figure 3: Observational measurement locations. Along-channel distance from the mouth of the estuary is determined using the PIR0701 sensor (most seaward diamond symbol) from the 2007 NOAA Piscataqua River Current Survey.

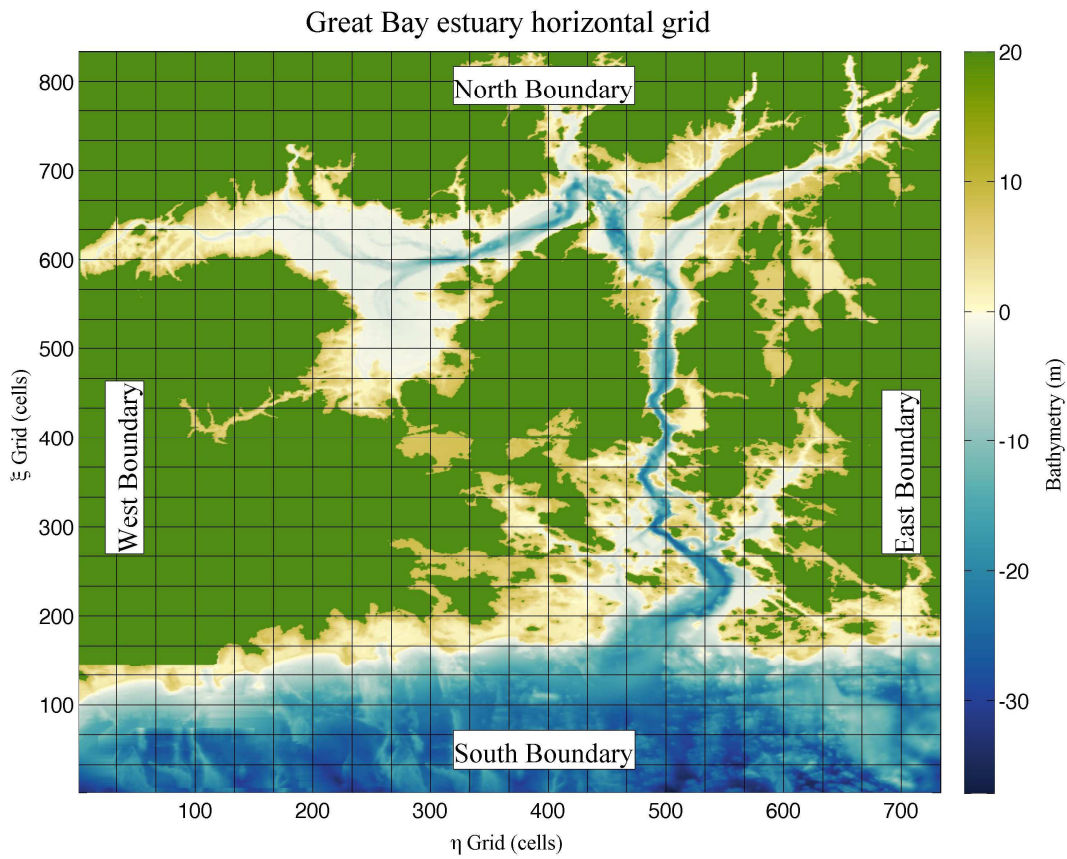


Figure 4: Rotated ROMS horizontal grid ( $\xi, \eta$ ) coordinates and model defined boundaries. Displayed gridlines are every 1 km, decimated by a factor of  $33 \frac{1}{3}$  from actual model grid (for display purposes). Cardinal directions of boundaries are relative to the orientation of the rotated grid.

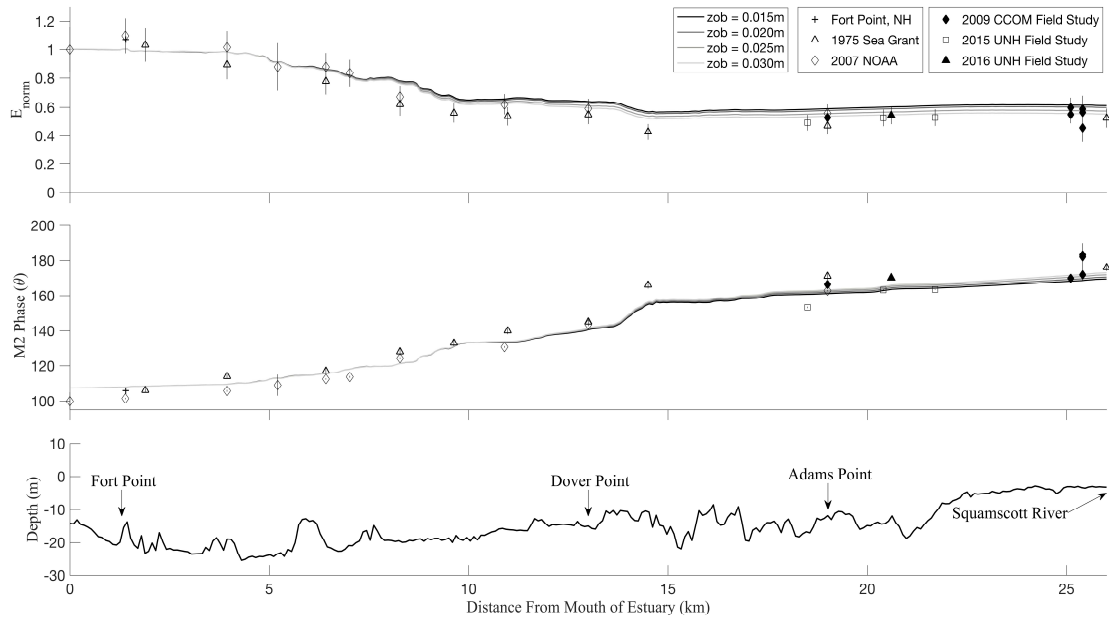


Figure 5: M2 tidal energy decay,  $E_{norm}$ , (upper panel) and phase evolution ( $deg$  Greenwich; middle panel) as a function of distance from the mouth of the estuary for different bottom roughness values ( $z_{ob}$ ) of the logarithmic drag law bottom boundary condition. Observations are included as symbols with error bars based on T\_TIDE analysis and following Taylor (1982). Depth profile along the center channel is shown in the lower panel with locations of Fort Point, Dover Point, Adams Point, and the Squamscott River are indicated.

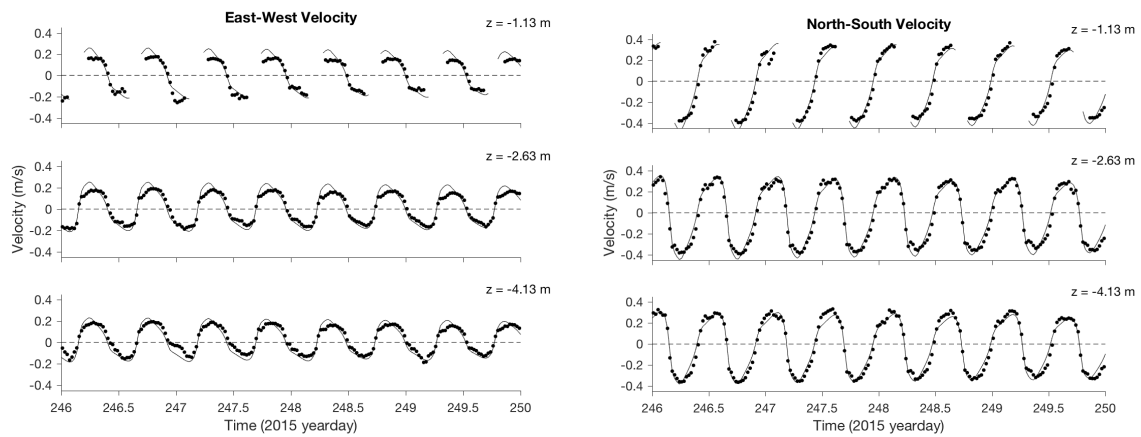


Figure 6. Modeled (dots) and observed (solid line) time series of east-west (left) and north-south (right) velocities from sensor located in 5.75 m water depth in the Great Bay. The vertical elevation relative to mean sea level (in  $m$ ) of each time series comparison is indicated on the right-hand-side of each panel. The discontinuous time series in the upper three panels are a result of tidal variations in water depth periodically exposing and inundating upper sensor locations near the sea surface. RMS errors range 0.035-0.049  $m/s$  and 0.047-0.055  $m/s$  for the east-west and north-south velocities, respectively.

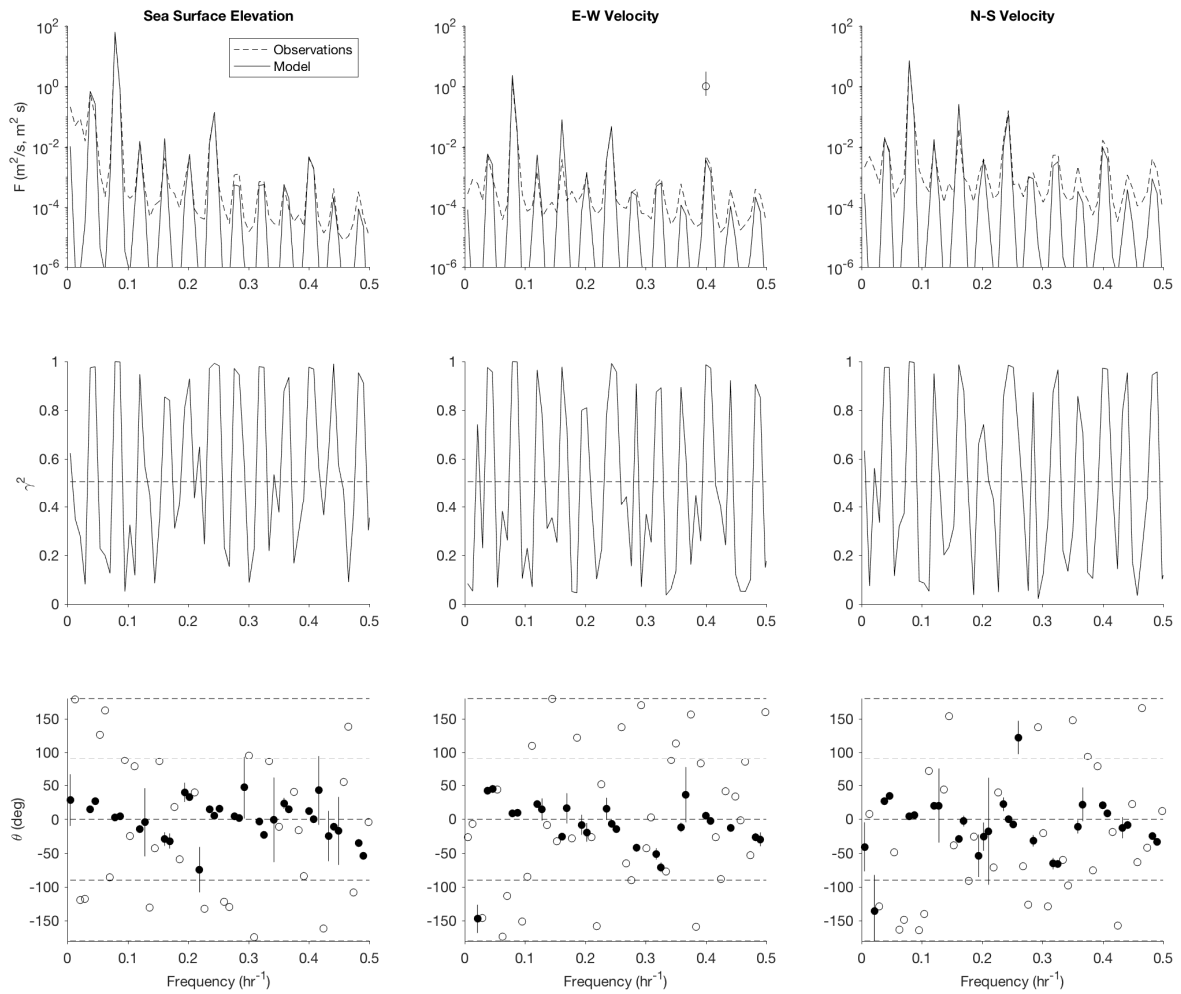


Figure 7. Cross-spectra between modeled and observed sea surface elevation (left panels), east-west depth-averaged velocity (center panels), and north-south depth-averaged velocity (right panels) for sensor location in 5.75  $m$  water depth in the Great Bay. Upper panels show spectral density,  $F$ , in  $m^2/s$  for sea surface elevation and  $m^2/s$  for velocities as a function of frequency ( $hr^{-1}$ ). Spectra were computed with a Hanning data window and 10 DOF. The 95% confidence interval is shown in the upper center panel. Observed spectra have a significantly higher noise floor but still below the energy levels of the harmonics. Center panels show the coherence squared,  $\gamma^2$ , with 95% significance level as the horizontal dashed line. Lower panels show the phase ( $deg$ ) with solid circles indicating significant phases with 95% confidence intervals.

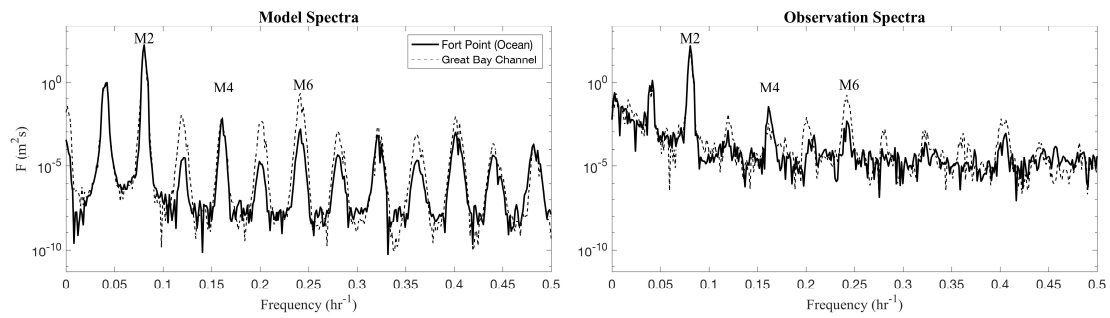


Figure 8: Modeled (left) and observed (right) spectral density,  $F$  ( $m^2/s$ ), of sea surface elevation from two stations, one near the mouth of the estuary (Fort Point; solid line) and one in 5.75 m water depth in the Great Bay (dotted line). Spectra show the growth of the tidal harmonics from the ocean to 20 km up the estuary (the M2, M4, and M6 constituents are indicated). Spectra were computed over a 30 day record and processed with a Hanning data window. Observed spectra have a significantly higher noise floor but still below the energy levels of the harmonics.

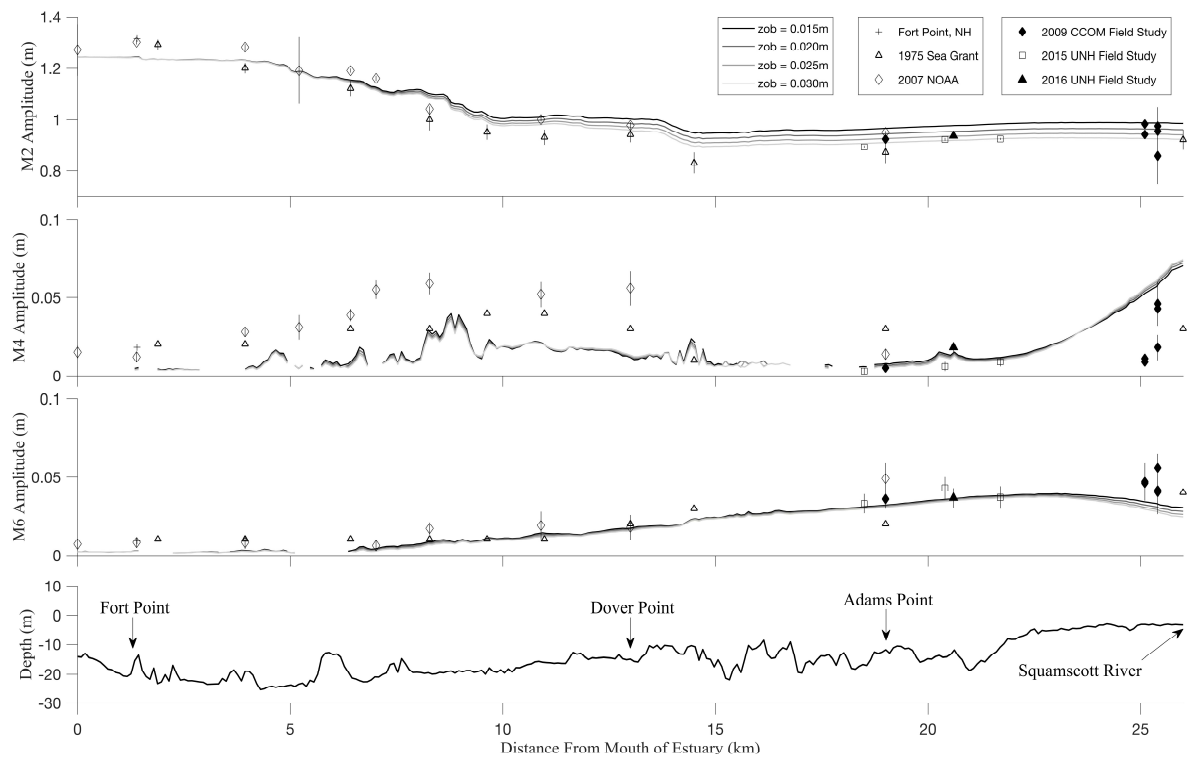


Figure 9: Modeled (lines) and observed (symbols) amplitude evolution of the M2 (top), M4 (2<sup>nd</sup> from top), and M6 (3<sup>rd</sup> from top) tidal constituents from Fort Point, near the mouth of the estuary, to the Great Bay. Amplitudes were determined with T\_TIDE analysis of 30+ day records (or for the 1975 data from the literature of which no error bars are available). Model results for a range of bottom roughness,  $z_{ob}$ , are indicated in the legend. The depth profile along the center channel is shown in the lower panel.



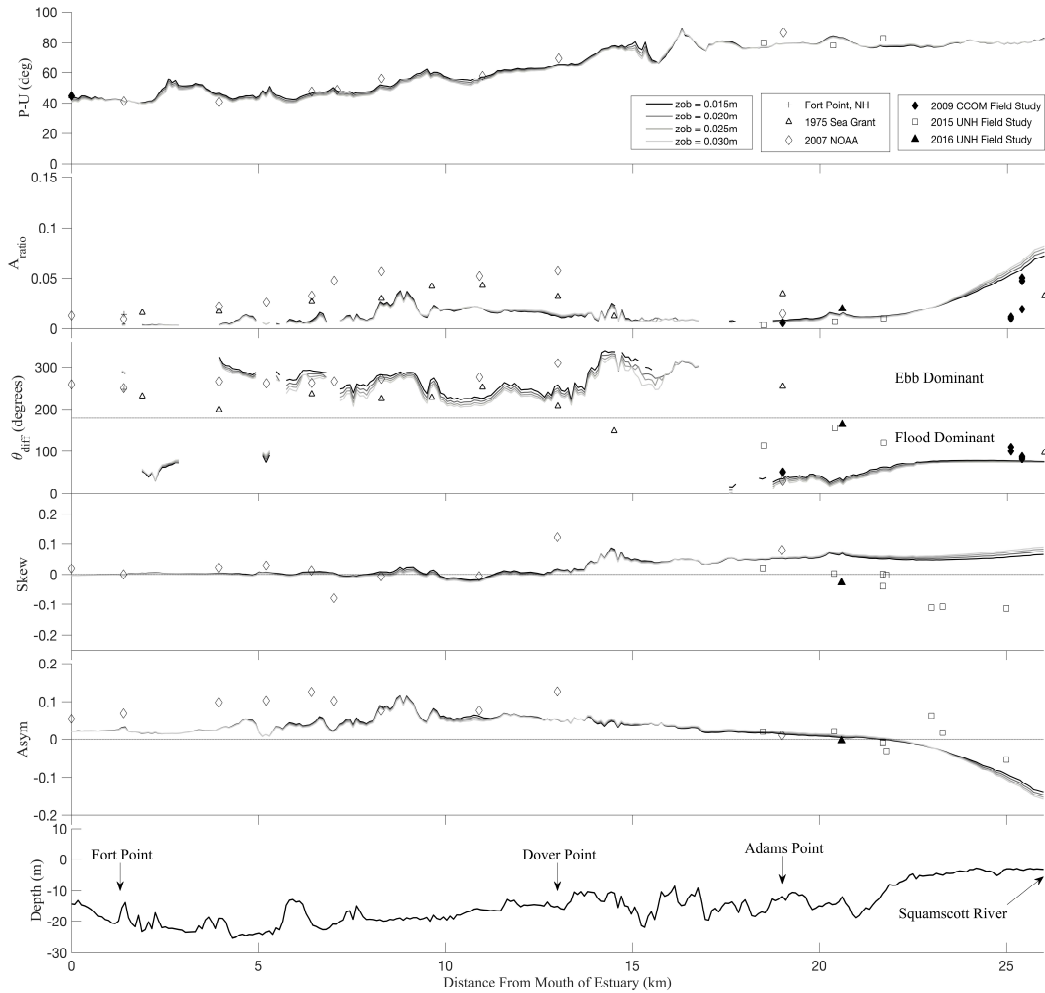


Figure 10. Modeled (lines) and observed (symbols) along-channel evolution of the  $P-U$  phase ( $deg$ ; top panel),  $A_{ratio}$  (2<sup>nd</sup> from top),  $\theta_{diff}$  (3<sup>rd</sup> from top; showing flood and ebb dominance), normalized skewness (4<sup>th</sup> from top), and normalized asymmetry (5<sup>th</sup> from top) of 30 day sea surface elevation time series from the ocean to the upper reaches of the Great Bay. The nonlinear evolution of the tide is clearly evident with the sea surface profile evolving from a partially progressive nearly sinusoidal form and ebb dominance between Fort Pt. and Dover Pt., to a nearly standing wave with highly skewed and pitched-forward shape and flood dominance in the Great Bay. Model results for a range of bottom roughness,  $z_{ob}$ , are indicated in the legend. The depth profile along the center channel is shown in the lower panel.

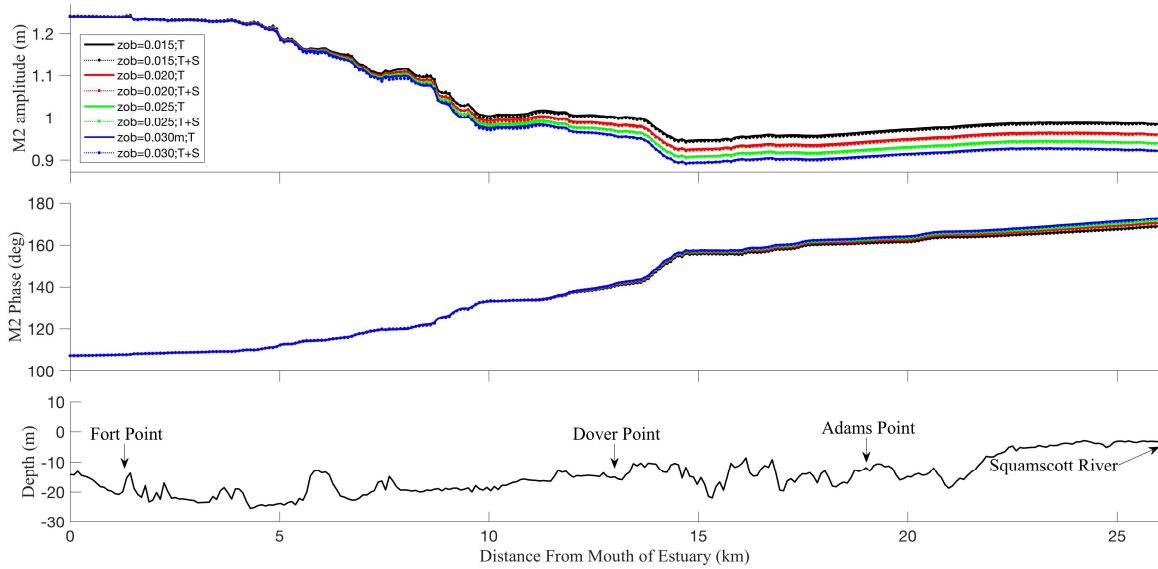


Figure 11. Modeled amplitude evolution for tidal only (solid lines) and tidal plus subtidal forcing (symbols) for the M2 tidal constituents from Fort Point, near the mouth of the estuary, to the Great Bay. Amplitudes were determined with T\_TIDE analysis of 30+ day records. Model results for a range of bottom roughness,  $z_{ob}$ , are indicated in the legend. The depth profile along the center channel is shown in the lower panel.

*\* This figure should be in color \**